Astronomy & Astrophysics manuscript no. schrabback_hawki_arxiv
January 22, 2019

Precise weak lensing constraints from deep high-resolution K_s images: VLT/HAWK-I analysis of the super-massive galaxy cluster RCS2 $J232727.7-020437$ at $z = 0.70^\star$

Tim Schrabback[1], Mischa Schirmer[2], Remco F. J. van der Burg[3,4], Henk Hoekstra[5], Axel Buddendiek[1], Douglas Applegate[1,6], Maruša Bradač[7], Tim Eifler[8,9], Thomas Erben[1], Michael D. Gladders[10,6], Beatriz Hernández-Martín[1], Hendrik Hildebrandt[1], Austin Hoag[7], Dominik Klaes[1], Anja von der Linden[11], Danilo Marchesini[12], Adam Muzzin[13], Keren Sharon[14], and Mauro Stefanon[5]

[1] Argelander-Institut für Astronomie, Universität Bonn, Auf dem Hügel 71, 53121, Bonn, Germany
e-mail: schrabba@astro.uni-bonn.de
[2] Gemini Observatory, Southern Operations Center, Casilla 603, La Serena, Chile
[3] IRFU, CEA, Université Paris-Saclay, F-91191 Gif-sur-Yvette, France
[4] Université Paris Diderot, AIM, Sorbonne Paris Cité, CEA, CNRS, F-91191 Gif-sur-Yvette, France
[5] Leiden Observatory, Leiden University, Niels Bohrweg 2, NL-2300 CA Leiden, The Netherlands
[6] Kavli Institute for Cosmological Physics, University of Chicago, 5640 South Ellis Avenue, Chicago, IL 60637
[7] Department of Physics, University of California, Davis, CA 95616, USA
[8] Jet Propulsion Laboratory, California Institute of Technology, 4800 Oak Grove Dr., Pasadena, CA 91109, USA
[9] Center for Cosmology and Astro-Particle Physics, The Ohio State University, 191 W. Woodruff Ave, Columbus, 43210 OH, USA
[10] Department of Astronomy and Astrophysics, University of Chicago, 5640 South Ellis Avenue, Chicago, IL 60637, USA
[11] Department of Physics and Astronomy, Stony Brook University, Stony Brook, NY 11794, USA
[12] Department of Physics and Astronomy, Tufts University, 574 Boston Avenue, Medford, MA 02155, USA
[13] Department of Physics and Astronomy, York University, 4700 Keele St., Toronto, Ontario, Canada, MJ3 1P3
[14] Department of Astronomy, University of Michigan, 1085 S. University Ave, Ann Arbor, MI 48109, USA

Received August 07, 2017; accepted October 26, 2017

ABSTRACT

We demonstrate that deep good-seeing VLT/HAWK-I K_s images complemented with g+z-band photometry can yield a sensitivity for weak lensing studies of massive galaxy clusters at redshifts $0.7 \lesssim z \lesssim 1.1$ that is almost identical to the sensitivity of HST/ACS mosaics of single-orbit depth. Key reasons for this good performance are the excellent image quality frequently achievable for K_s imaging from the ground, a highly effective photometric selection of background galaxies, and a galaxy ellipticity dispersion that is noticeably lower than for optically observed high-redshift galaxy samples. Incorporating results from 3D-HST and UltraVISTA we also obtain a more accurate calibration of the source redshift distribution than previously achieved for similar optical weak lensing data sets. Here we study the extremely massive galaxy cluster RCS2 $J232727.7-020437$ ($z = 0.699$), combining deep VLT/HAWK-I K_s images (PSF FWHM = 0.″35) with LBT/LBC photometry. The resulting weak lensing mass reconstruction suggests that the cluster consists of a single overdensity, which is detected with a peak significance of 10.1σ. We constrain the cluster mass to $M_{200c}/(10^{15}\mathrm{M}_\odot) = 2.06^{+0.28}_{-0.26}(\mathrm{stat.}) \pm 0.12(\mathrm{sys.})$ assuming a spherical NFW model and simulation-based priors on the concentration, making it one of the most massive galaxy clusters known in the $z \gtrsim 0.7$ Universe. We also cross-check the HAWK-I measurements through an analysis of overlapping HST/ACS images, yielding fully consistent estimates of the lensing signal.

Key words. Gravitational lensing: weak; Galaxies: clusters: individual: RCS2 $J232727.7-020437$.

1. Introduction

Light bundles from distant galaxies are distorted by the tidal gravitational field of foreground structures. These weak lensing distortions can be constrained statistically from the observed shapes of background galaxies, providing information on the differential projected mass distribution of the foreground objects, free of assumptions on their dynamical state (e.g. Bartelmann & Schneider 2001). To conduct such measurements, sufficiently unbiased estimates of galaxy shapes have to be obtained, corrected for the impact of the image point-spread function (PSF). This is only possible if the observed galaxy images are sufficiently resolved, as the blurring PSF otherwise erases the shape information. Weak lensing observations therefore benefit from good image quality, which boosts the number density of sufficiently resolved galaxies and thus the signal-to-noise ratio, while simultaneously reducing the required level of PSF corrections and therefore systematic uncertainties (e.g. Massey et al. 2013).

For studies targeting more distant lenses it is vital to employ deep observations with superb image quality to measure the shapes of the typically faint and small distant background galaxies carrying the signal. In red optical filters, queue-scheduled ground-based observations from the best sites achieve a stel-

* Based on observations conducted with the ESO Very Large Telescope, the Large Binocular Telescope, and the NASA/ESA *Hubble* Space Telescope, as detailed in the acknowledgements.

lar PSF Full-Width at Half-Maximum (FWHM*) $\simeq$ 0.″6–0.″7 in good conditions (e.g. Kuijken et al. 2015; Mandelbaum et al. 2017), which provides a good weak lensing sensitivity out to lens redshifts $z \sim 0.6$ in the case of deep integrations. Much higher resolution (FWHM* $\simeq$ 0.″10) can be achieved with the *Hubble* Space Telescope (HST), which has been used to probe the weak lensing signatures out to significantly higher redshifts when targeting galaxies (Leauthaud et al. 2012), galaxy clusters (e.g. Jee et al. 2011; Schrabback et al. 2017, S17 henceforth), or the statistical properties of the large-scale structure itself (Massey et al. 2007; Schrabback et al. 2010). However, HST has a relatively small field-of-view of 3.′3 × 3.′3 for its ACS/WFC detector, raising the need for time-consuming mosaics in order to cover a wider area on the sky. In particular, studies that aim to obtain accurate weak lensing mass measurements for massive galaxy clusters at moderately high redshifts ($0.7 \lesssim z \lesssim 1.1$), have so far required mosaic ACS images to probe the lensing signal out to approximately the cluster virial radius (e.g. S17; Jee et al. 2009; Thölken et al. 2017).

In this paper we demonstrate that deep ground-based imaging obtained in the HAWK-I K_s filter ($1.98\mu\mathrm{m} \lesssim \lambda \lesssim 2.30\mu\mathrm{m}$) under good seeing conditions can provide a viable alternative to mosaic HST observations for moderately deep weak lensing measurements. The observational setup we describe provides several advantages for weak lensing studies. First, for an 8m-class telescope and typical conditions, the measured atmospheric PSF FWHM is reduced by $\simeq 40\%$ at such long wavelengths compared to the V band (Martinez et al. 2010). As a result, delivered image qualities of FWHM* $\simeq$ 0.″3–0.″4 are achieved in K_s in good conditions without having to request the very best seeing quantile. While not quite reaching an HST-like resolution, this still provides a major advantage for weak lensing measurements compared to optical seeing-limited observations. The second advantage is the efficiency of selecting distant background sources in K (or K_s)-detected galaxy samples, using the "*BzK* selection" technique (Daddi et al. 2004) with observations taken in three bands only. As a third advantage, excellent deep NIR-selected reference samples have recently become available to infer the redshift distribution of the weak lensing source galaxies, including photometric redshifts from UltraVISTA (McCracken et al. 2012; Muzzin et al. 2013; Muzzin et al. in prep.) and HST slitless spectroscopy from the 3D-HST programme (Momcheva et al. 2016). Finally, at $z \sim 2$ K_s imaging probes the light distribution of the smoother stellar component exhibiting lower shape noise, an advantage over optical imaging which mostly maps the clumpy distribution of star forming regions seen at rest-frame UV wavelengths.

In this study we analyse new deep VLT/HAWK-I K_s observations of the galaxy cluster RCS2 *J*232727.7−020437 (hereafter: RCS2 *J*2327; $z = 0.699$, Sharon et al. 2015) discovered in the Second Red-Sequence Cluster Survey (RCS2; Gilbank et al. 2011). Optical, Sunyaev-Zel'dovich, X-ray, dynamical, strong lensing, and initial weak lensing measurements of the cluster are consistent with an extremely high mass of $M_{200\mathrm{c}} \simeq 2\text{–}3 \times 10^{15}\mathrm{M}_\odot$ (Menanteau et al. 2013; Sharon et al. 2015; Buddendiek et al. 2015; Hoag et al. 2015), where $M_{\Delta\mathrm{c}}$ indicates the mass within the sphere containing an average density that exceeds the critical density of the Universe at the cluster redshift by a factor Δ. Hence, it is one of the most massive clusters known at a comparable or higher redshift.

King et al. (2002) presented the first, and previously only weak lensing analysis based on shape measurements in K_s images. Their analysis targeting a massive low-redshift cluster is based on imaging obtained with SofI on the 3.6m ESO-NTT with an image resolution of 0.″73. Our analysis exploits much deeper K_s imaging with a resolution that is better by a factor two, as needed for high-redshift weak lensing constraints. We explicitly compare the weak lensing performance achieved with these new K_s data to the weak lensing analysis of galaxy clusters at similar redshift from S17. They employed 2×2 HST/ACS mosaics of single-orbit depth taken in the F606W filter for shape measurements, and a photometric source selection based on $V_{606} - I_{814}$ colour to remove cluster galaxies and preferentially select distant background galaxies.

This paper is organised as follows: We summarise relevant weak lensing theory and notation in Sect. 2. Sect. 3 describes the analysed data sets and data reduction. Sect. 4 provides details on the shape and colour measurements, the background selection, the estimation of the source redshift distribution, an analysis of the galaxy ellipticity dispersion, and a comparison to shear estimates from HST measurements. Sect. 5 presents the cluster mass reconstruction, the derived cluster mass constraints, and the comparison to previous studies of the cluster. We compare the weak lensing performance of the HAWK-I data and the previously employed ACS mosaics in Sect. 6 and conclude in Sect. 7.

Throughout this paper we assume a flat ΛCDM cosmology characterised through $\Omega_\mathrm{m} = 0.3$, $\Omega_\Lambda = 0.7$, $H_0 = 70\,h_{70}\,\mathrm{km\,s^{-1}}$ and $h_{70} = 1$, as approximately consistent with recent constraints from the Cosmic Microwave Background (e.g. Hinshaw et al. 2013; Planck Collaboration et al. 2016), unless explicitly stated otherwise. At the cluster redshift of $z = 0.699$, 1″ on the sky corresponds to a physical separation of 7.141 kpc in this cosmology. All magnitudes are in the AB system.

2. Summary of relevant weak lensing theory

In the weak lensing regime the gravitational lensing effect of a lens at redshift z_l (assumed to be fixed here) onto the shape of a background galaxy at redshift z_s and an observed position $\boldsymbol{\theta}$ can be described through the anisotropic reduced shear

$$g(\boldsymbol{\theta}, z_\mathrm{s}) = \frac{\gamma(\boldsymbol{\theta}, z_\mathrm{s})}{1 - \kappa(\boldsymbol{\theta}, z_\mathrm{s})}\,, \tag{1}$$

which is a re-scaled version of the unobservable shear $\gamma(\boldsymbol{\theta}, z_\mathrm{s})$, and the isotropic convergence

$$\kappa(\boldsymbol{\theta}, z_\mathrm{s}) = \Sigma(\boldsymbol{\theta})/\Sigma_\mathrm{crit}(z_\mathrm{l}, z_\mathrm{s}) \tag{2}$$

(see e.g. Bartelmann & Schneider 2001 for a general review and Hoekstra et al. 2013 for applications to clusters). The latter is defined as the ratio of the surface mass density $\Sigma(\boldsymbol{\theta})$ and the critical surface mass density

$$\Sigma_\mathrm{crit}(z_\mathrm{l}, z_\mathrm{s}) = \frac{c^2}{4\pi G}\frac{1}{D_\mathrm{l}(z_\mathrm{l})\beta(z_\mathrm{l}, z_\mathrm{s})}, \tag{3}$$

where c and G are the speed of light and the gravitational constant, respectively, while D_l denotes the angular diameter distance to the lens. The geometric lensing efficiency

$$\beta(z_\mathrm{l}, z_\mathrm{s}) = \max\left[0, \frac{D_\mathrm{ls}(z_\mathrm{l}, z_\mathrm{s})}{D_\mathrm{s}(z_\mathrm{s})}\right] \tag{4}$$

is defined in terms of the angular diameter distances from the observer to the source D_s, and from the lens to the source D_ls.

Given that they are both computed from second-order derivatives of the lensing potential, the weak lensing shear γ and convergence κ are linked. The spatial distribution of the convergence

can therefore be reconstructed from the shear field up to an integration constant (Kaiser & Squires 1993), which represents the mass-sheet degeneracy (Schneider & Seitz 1995).

Weak lensing shape measurement algorithms aim to obtain unbiased estimates of the complex galaxy ellipticity

$$\epsilon = \epsilon_1 + \mathrm{i}\epsilon_2 = |\epsilon| \mathrm{e}^{2\mathrm{i}\varphi} \,. \tag{5}$$

In the idealised case of an object that has concentric elliptical isophotes with a constant position angle φ and constant ratios of the semi-major and semi-minor axes a and b, these are related to the ellipticity as $|\epsilon| = (a-b)/(a+b)$. The ellipticity transforms under weak reduced shears ($|g| \ll 1$) as

$$\epsilon \simeq \epsilon_\mathrm{s} + g \tag{6}$$

(for the general case see Seitz & Schneider 1997; Bartelmann & Schneider 2001). The intrinsic source ellipticity ϵ_s is expected to have a random orientation, yielding an expectation value $\langle \epsilon_\mathrm{s} \rangle = 0$. Hence, ellipticity measurements provide noisy estimates for the local reduced shear, where the noise level is given by the dispersion

$$\sigma_\epsilon = \sigma\left(\epsilon - g\right) \simeq \sqrt{\sigma_\mathrm{int}^2 + \sigma_\mathrm{m}^2} \,, \tag{7}$$

which has contributions from both the intrinsic ellipticity dispersion $\sigma_\mathrm{int} = \sigma\left(\epsilon_\mathrm{s}\right)$ of the galaxy sample[1] and measurement noise σ_m (e.g. Leauthaud et al. 2007, S17). Assuming dominant shape noise, the signal-to-noise ratio of the detection of the weak lensing reduced shear signal scales as

$$\left(\frac{S}{N}\right)_\mathrm{WL} \propto f \equiv \frac{\sqrt{n_\mathrm{gal}}\langle\beta\rangle}{\sigma_{\epsilon,\mathrm{eff}}} \,, \tag{8}$$

where n_gal indicates the weak lensing source density on the sky and $\sigma_{\epsilon,\mathrm{eff}}$ corresponds to the effective value of σ_ϵ computed taking possible shape weights into account. The weak lensing signal-to-noise ratio also depends on the mass, the mass distribution, and the radial fitting range (e.g. Bartelmann & Schneider 2001). Shape weights w_i also need to be taken into account when computing $\langle\beta\rangle$, where we employ magnitude-dependent weights

$$w_i(\mathrm{mag}_i) = \sigma_\epsilon^{-2}(\mathrm{mag}_i) \,, \tag{9}$$

which are directly related to the expected noise in the reduced shear estimate for galaxy i. In this case the effective ellipticity dispersion for the sample from Eq. 8 reads

$$\sigma_{\epsilon,\mathrm{eff}} = \left(N^{-1}\sum_{i=1}^{N} w_i\right)^{-\frac{1}{2}} \,. \tag{10}$$

For cluster weak lensing analyses it is useful to decompose the ellipticity (and likewise the reduced shear) into a tangential component carrying the signal

$$\epsilon_\mathrm{t} = -\epsilon_1 \cos 2\phi - \epsilon_2 \sin 2\phi \,, \tag{11}$$

where ϕ denotes the azimuthal angle with respect to the cluster centre, as well as the 45 degrees-rotated "cross-component"

$$\epsilon_\times = +\epsilon_1 \sin 2\phi - \epsilon_2 \cos 2\phi \,. \tag{12}$$

The averaged tangential ellipticity profile provides an estimate for the tangential reduced shear profile $g_\mathrm{t}(r)$ of the cluster, which we fit using model predictions from Wright & Brainerd (2000) that assume a spherical NFW density profile (Navarro et al. 1997).

[1] We absorb the effective broadening of the observed ellipticity distribution due to cosmological weak lensing by uncorrelated large-scale structure in σ_int. In Eq. 7 g refers to the reduced shear caused by the targeted cluster.

3. Data and data reduction

In our analysis we make use of high-resolution VLT/HAWK-I K_s images for the weak lensing shape measurements, which we complement with LBT/LBC imaging for a colour selection. We additionally analyse overlapping HST/ACS data to cross-check the VLT/HAWK-I weak lensing constraints.

3.1. VLT/HAWK-I data

RCS2 J2327 was observed with VLT UT4 using HAWK-I under programme 087.A-0933 (PI: Schrabback). HAWK-I is a high-throughput Near-Infrared (NIR) imager equipped with a 2×2 mosaic of 2048×2048 Rockwell HgCdTe MBE HAWAII 2 RG arrays, with a plate-scale of $0\farcs106$ pixel^{-1} and a $7\farcm5 \times 7\farcm5$ field-of-view (see Kissler-Patig et al. 2008, for details). Here we analyse K_s band images observed using large dither steps to cover the $\sim 15''$ gaps between the detectors. In total, 326×80 s exposures were obtained (total exposure time 7.2h), some of which were repetitions because the seeing constraint (K_s band image quality $\leq 0\farcs4$) was not fulfilled. Each 80 s exposure was constructed from 8×10 s internal sub-exposures to avoid background saturation, averaged using on-detector arithmetics.

The data were reduced using `THELI` (Erben et al. 2005; Schirmer 2013) following standard procedures, including dark subtraction and flat fielding. A dynamic 2-pass background subtraction including object masking was employed to remove the sky background from individual exposures. The background models were calculated from a floating median of the 8 closest images in time, corresponding to a time window of 13 – 15 minutes. An accurate astrometric reference catalogue is required to align the images on sky. The 2MASS catalogue has insufficient source density for this purpose, as RCS2 J2327 is located at high galactic latitude of −58°. Thus, we first processed and co-added CFHT Megaprime i band data (PI: H. Hoekstra), for which an astrometric calibration was possible using 2MASS thanks to the larger field-of-view. We then extracted a deep astrometric reference catalogue from the CFHT data, which was used both for the HAWK-I reduction and the reductions described in Sections 3.2 and 3.3. The astrometry for the HAWK-I data was determined by `THELI` using `Scamp` (Bertin 2006). The relative positions of the detectors were accurately fixed using the dithered exposures, and a fixed third-order distortion polynomial was used to describe the non-linear terms. In total, relative image registration is accurate to $\sim$ 1/10-th of a pixel, well sufficient for our shear analysis. Image co-addition and resampling in `THELI` was performed with `SWarp` (Bertin et al. 2002), using a Lanczos3 kernel matched to the well-sampled PSF.

Given the variation in seeing we created two separate stacks. The first stack is generated from all exposures for photometric measurements, yielding a total integration time of 26.1 ks and a median stellar FWHM* = $0\farcs40$ as measured by `SExtractor` (Bertin & Arnouts 1996). The second stack is used for the shape measurements. Here we exclude exposures with poorer image quality, yielding a shorter total integration time of 17.1 ks (4.8 h, or $\sim$ 7 h including overheads), but a better image quality with a median FWHM* = $0\farcs35$. To simplify the comparison to the weak lensing literature we also report the median stellar FLUX_RADIUS parameter from `SExtractor` $r_\mathrm{f}^* = 0\farcs22$ and the median stellar half-light radius from `analyseldac` (Erben et al. 2001) $r_\mathrm{h}^* = 0\farcs19$.

3.2. LBT/LBC data

RCS2 J2327 was also observed by the Large Binocular Telescope (LBT) on Oct 02, 2010 (PI: Eifler) under good seeing conditions ($\simeq 0\farcs7$), where we make use of g-band observations obtained with LBC_BLUE (Giallongo et al. 2008) and z-band observations obtained with LBC_RED. The data were reduced using `THELI` following standard procedures, yielding co-added total integration times of 2.4 ks in the g band and 3.0 ks in the z band.

3.3. HST/ACS data

To cross-check our HAWK-I shape measurements we also reduce and analyse HST/ACS observations (HST-GO 13177, PI: Bradač) of RCS2 J2327 conducted with the F814W filter as part of the Spitzer Ultra Faint SUrvey Program (Bradač et al. 2014). This includes a central pointing (integration time 5.6 ks), as well as four parallel fields (integration times 3.6–5.5 ks) which overlap with the outskirts of our HAWK-I observations. In order to generate a colour image we also process central ACS observations conduced in the F435W filter (integration time 4.2 ks) as part of the HST-GO programme 10846 (PI: Gladders).

We reduce these data employing the pixel-level correction for charge-transfer inefficiency from Massey et al. (2014), the standard ACS calibration pipeline `CALACS` for further basic reduction steps, `MultiDrizzle` (Koekemoer et al. 2003) for the cosmic ray removal and stacking, as well as scripts from Schrabback et al. (2010) for the image registration and optimisation of masks and weights.

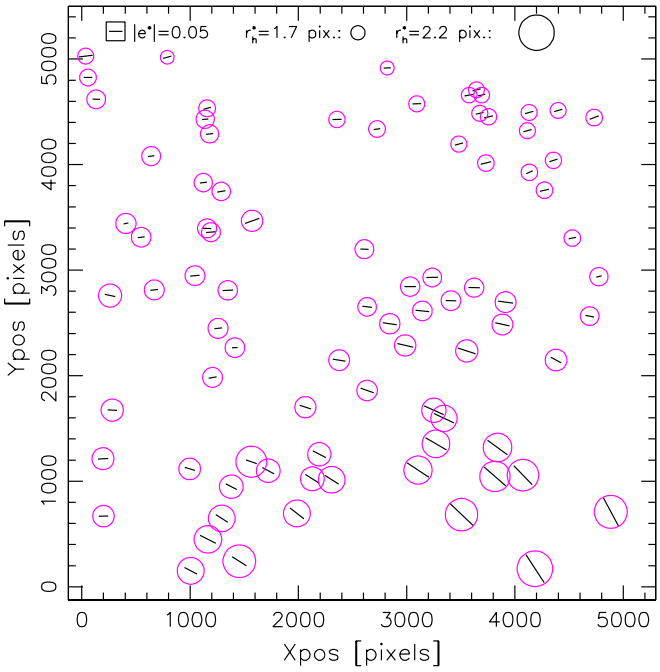

Fig. 1. Spatial variation of the PSF in our best-seeing stack of the HAWK-I K_s observations of RCS2 J2327: Each whisker indicates the measured polarisation e^* of a star, while the circle indicates its half-light radius r_h^* from `analyseldac` (see the reference whisker and circles at the top for the absolute scale). In this stack North is up and East is left, matching the orientation of the input frames (observations obtained with a default 0° position angle).

4. Analysis

4.1. HAWK-I shape measurements

We detect objects with `SExtractor` and measure weak lensing shapes using the `analyseldac` (Erben et al. 2001) implementation of the KSB+ formalism (Kaiser et al. 1995; Luppino & Kaiser 1997; Hoekstra et al. 1998) as detailed in Schrabback et al. (2007), employing the correction for multiplicative noise bias as a function of the `analyseldac` signal-to-noise ratio from Schrabback et al. (2010). Analysing the measured shapes of stellar images in our K_s best-seeing stack we find that the HAWK-I PSF is well-behaved in the majority of the field-of-view with PSF polarisation amplitudes $|e^*| \lesssim 0.05$, where

$$e = e_1 + \mathrm{i}e_2 = \frac{Q_{11} - Q_{22} + 2\mathrm{i}Q_{12}}{Q_{11} + Q_{22}} \tag{13}$$

is defined via weighted second-order brightness moments Q_{ij} as detailed in Schrabback et al. (2007). However, the PSF degrades noticeably towards lower y positions with larger stellar polarisations and half-light radii r_h^* as computed by `analyseldac` (see Figure 1). We find that the spatial variations of the KSB+ PSF parameters can be interpolated well using third-order polynomials combining stars from all chips. For the weak lensing analysis we require galaxies to be sufficiently resolved with half-light radii $r_h > 1.2 r^*_{h,\mathrm{mod}}(x,y)$, where $r^*_{h,\mathrm{mod}}(x,y)$ indicates the polynomial interpolation of the measured stellar half-light radii at the position of the galaxy. We select galaxies having a flux signal-to-noise ratio defined via the auto flux from `SExtractor` of $(S/N)_{\mathrm{flux}} = \mathrm{FLUX\_AUTO/FLUXERR\_AUTO} > 10$. Shape selections are also applied according to the trace of the "pre-seeing" shear polarisability tensor $\mathrm{Tr}P^g/2 > 0.1$ and PSF-corrected ellipticity estimate $|\epsilon| < 1.4$. We mask regions around bright foreground objects and reject galaxies that are flagged by `SExtractor` or `analyseldac`, e.g. due to the presence of a nearby object. Prior to the photometric background selection our catalogue of galaxies with weak lensing shape estimates has a source number density of 45 arcmin^{-2}.

Analysing ACS-like image simulations containing weak simulated shears ($|g| < 0.06$), Schrabback et al. (2010) estimate that the basic shape measurement algorithm employed also in our current work leads to residual multiplicative shear biases $|m| < 2\%$. However, they neither tested the performance in the stronger shear regime of clusters nor the sensitivity to the assumed input ellipticity distribution of galaxies, which can affect measured noise biases (Viola et al. 2014; Hoekstra et al. 2015). We have therefore conducted additional tests using new simulations created with `galsim` (Rowe et al. 2015). The details of these tests will be described in Hernández-Martín et al. (in prep.). For our current work the most relevant result from these simulations is that multiplicative biases are limited to $|m| \lesssim 3\%$ for reduced shears $|g| < 0.2$ and variations in the intrinsic ellipticity dispersion in the range $0.2 \leq \sigma_{\mathrm{int}} \leq 0.3$. For stronger shear $|g| < 0.4$ biases are limited to $|m| \lesssim 5\%$, still without re-calibration compared to the work from Schrabback et al. (2010). Given that most of the weak lensing mass constraints for RCS2 J2327 originate from scales with $|g| < 0.2$, while the innermost radial bins that are included have $|g| < 0.4$ (see Sect. 5), we assume an intermediate 4% systematic uncertainty on the shear calibration for our systematic error budget. Based on the analysis from Hernández-Martín et al. (in prep.) we conclude that this shear calibration uncertainty results from a combination of limitations in the noise bias correction and a slight non-linear response of our KSB+ implementation for stronger shears, both

of which can be fixed with a re-calibration for potential future studies requiring a tighter systematic error control.

4.2. Photometry

For the HAWK-I K_s data all photometric measurements are conducted on the stack derived from all available exposures (see Sect. 3.1). We homogenise the PSF between the VLT and LBT stacks using spatially varying kernels constructed using `PSFEx` (Bertin 2011) and measure colours between these PSF-homogenised images employing 2.″0 diameter circular apertures. We use 2MASS (Skrutskie et al. 2006) K_s magnitudes for the absolute photometric calibration of the HAWK-I data. For the g and z bands we initially estimate zero-points with respect to K_s using stellar locus regression. We then apply residual zero-point offsets to optimise the overlap of the galaxy colour distributions in $g - z$ versus $z - K_s$ colour space between our catalogue and the UltraVISTA-detected reference catalogue used to estimate the redshift distribution (see Sect. 4.3)[2]. Photometric errors are estimated from the flux fluctuations when placing apertures at random locations that do not contain detected objects. For the 2.″0 diameter apertures we compute median 5σ limiting magnitudes[3] of (26.6, 25.9, 25.0) in the (g, z, K_s) bands. For the subsequent analysis we exclude regions near the edges of the HAWK-I mosaic and the LBT chip gaps as they have a significantly reduced depth in some of the bands. We also limit the subsequent analysis to galaxies with `SExtractor` "auto" magnitudes in the range $21 < K_s^{tot} < 24.2$, given that brighter magnitude bins contain very few background galaxies, while the sample becomes highly incomplete at fainter magnitudes given the shape cuts (compare to the top panel of Fig. 2).

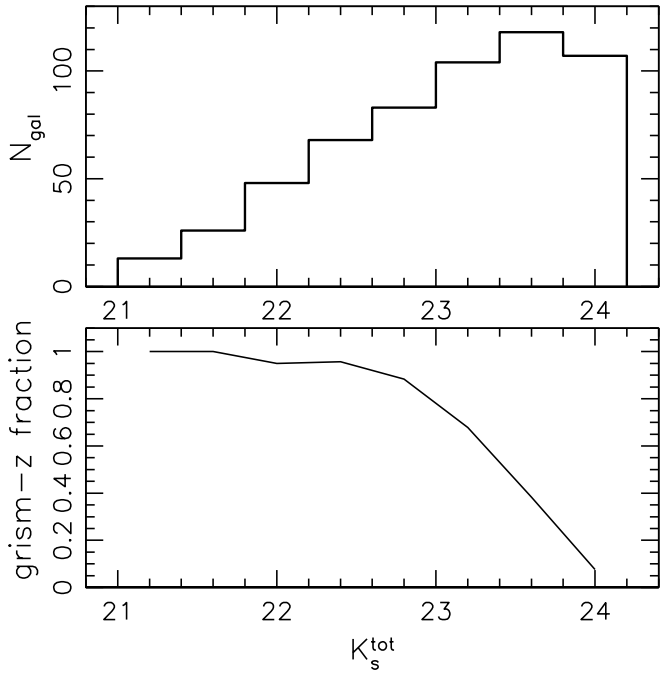

Fig. 2. *Top:* Histogram of the number of colour-selected galaxies in our HAWK-I weak lensing shape catalogue (covering a non-masked area of 52.4 arcmin^2) as a function of the total K_s magnitude. *Bottom:* Fraction of colour-selected galaxies within the CANDELS/COSMOS 3D-HST grism area with a robust HST grism redshift or spectroscopic redshift as a function of the total K_s magnitude from UltraVISTA.

4.3. Reference samples to estimate the source redshift distribution

For unbiased mass measurements we have to accurately estimate the weighted-average geometric lensing efficiency $\langle\beta\rangle$ (see Eq. 4) of the selected source sample. Here, a photometric selection of the lensed background galaxies helps to increase the measurement sensitivity, while reducing systematic uncertainties arising from cluster member contamination. Similar to the strategy from S17 we employ a colour selection (see Sect. 4.4) that is designed to yield negligible residual contamination by cluster members and apply a consistent selection to well-calibrated reference data from deep fields to estimate the redshift distribution and $\langle\beta\rangle$ (see Sect. 4.5).

4.3.1. UltraVISTA reference catalogue

The UltraVISTA Survey (McCracken et al. 2012) has obtained very deep NIR imaging in the COSMOS field (Scoville et al. 2007). By design the greatest depth is achieved in the "ultra-deep" stripes (McCracken et al. 2012), reaching a 5σ limiting K_s magnitude in 2.″0 apertures of 25.2 in the latest DR3 release, which exceeds even the depth of our HAWK-I imaging by 0.2 mag. COSMOS/UltraVISTA allows us to investigate galaxy colour and redshift distributions for our weak lensing analysis, where the 50 times larger area compared to HAWK-I (~ 0.75 deg^2) greatly reduces uncertainties from sampling variance (see Sect. 4.5). In particular, we employ an updated version of the K_s-selected photometric redshift catalogue from Muzzin et al. (2013) that makes use of the deeper UltraVISTA DR3 data (see Muzzin et al. in prep. for details). In addition to the PSF-matched aperture magnitudes in g, z, and K_s used for colour measurements, we make use of the `SExtractor` "auto" magnitudes K_s^{tot}. For our study we limit the analysis to objects that are photometrically classified as galaxies, located in non-masked areas of the "ultra-deep" stripes, and that are not flagged as blends by `SExtractor`.

While our HAWK-I+LBC catalogue and the UltraVISTA-detected catalogue have the same median depth in g (within 0.05 mag), the UltraVISTA-detected catalogue is deeper by 0.2 mag in K_s and shallower by 0.5 mag in z. We expect that the small difference in K_s depth is negligible for our analysis, but to further improve the matching in the source selection between the two catalogues, we add Gaussian noise to the UltraVISTA K_s^{tot} magnitudes to have identical limiting magnitudes (note that we also explicitly account for the incompleteness of the lensing catalogue when computing $\langle\beta\rangle$ in Sect. 4.5.1). The impact of differences in the noise in the colour measurement is investigated in Sect. 4.5.3.

4.3.2. 3D-HST reference catalogue

As a second reference data set to infer the source redshift distribution we employ redshifts computed by the 3D-HST team for galaxies in the CANDELS (Grogin et al. 2011) area within the COSMOS field. This includes HST/NIR-selected photometric redshifts based on a total of 44 different photometric data sets

[2] This is necessary for two reasons. First, differences in the effective filter curves between our HAWK-I+LBC data and the VISTA+Subaru data used for UltraVISTA reference catalogue lead to small differences in the colour calibration for stars and galaxies. Second, small zero-point offsets have already been applied to the UltraVISTA reference catalogue to improve the photo-z performance (see Muzzin et al. 2013).

[3] We quote limiting magnitudes without aperture correction.

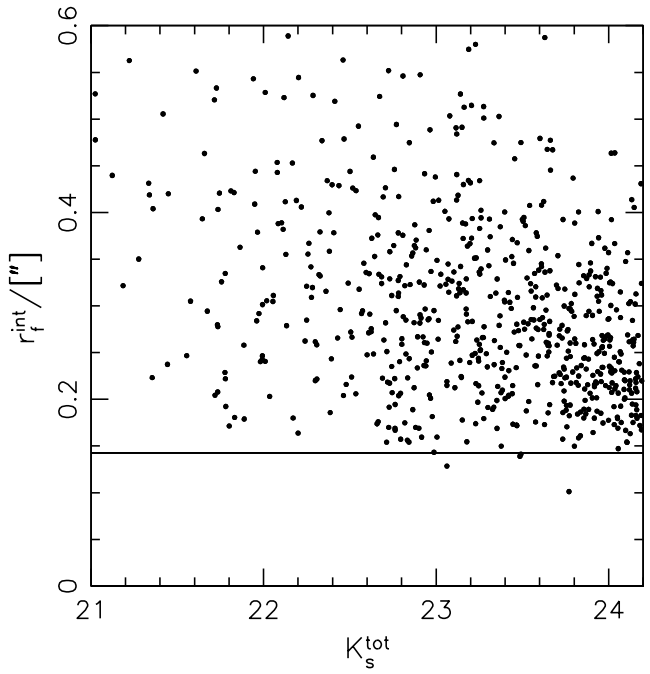

Fig. 3. Intrinsic flux radius r_f^{int} as measured in HST/WFC3 H-band data for galaxies in the CANDELS/COSMOS 3D-HST grism area passing our colour selection as a function of K_s^{tot}. The horizontal line corresponds to the mean size cut in our HAWK-I weak lensing analysis.

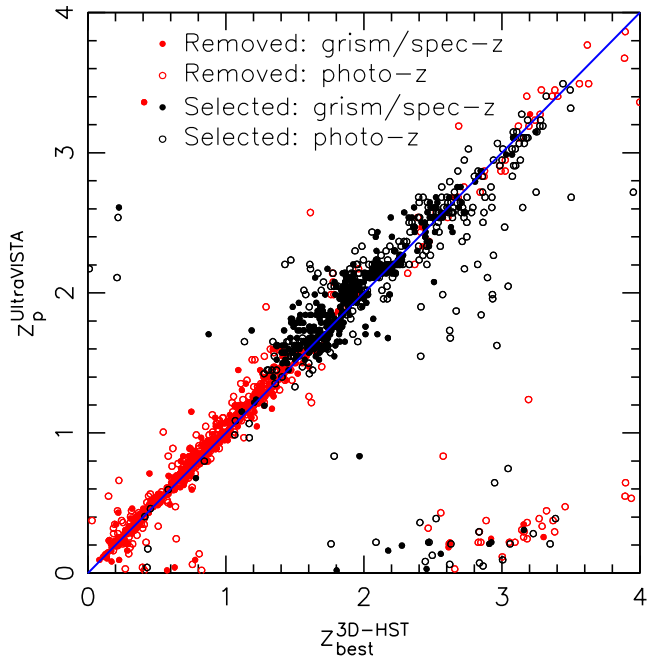

Fig. 4. Comparison of the best redshift estimate z_{best} from 3D-HST and the peak photometric redshift z_p in the UltraVISTA-detected catalogue for galaxies located in the area covered by the grism observations with $21 < K_s^{tot} < 24.2$. Galaxies with a spectroscopic or grism redshift in the 3D-HST catalogue are marked as filled circles, while the galaxies having a photometric redshift in the 3D-HST catalogue only are shown as open circles. Black symbols correspond to galaxies passing our colour selection, while red symbols show galaxies removed by the colour selection. The blue line shows the one-to-one relation.

(Skelton et al. 2014), as well as "grism"-redshift estimates from WFC3/IR slitless spectroscopy (Momcheva et al. 2016), where we also include ground-based spectroscopic redshifts compiled in the 3D-HST catalogue. Given the deeper NIR photometry and the deep grism spectra, these redshifts are expected to be highly robust, allowing us to conduct important cross-checks for our analysis. After applying our magnitude and colour selection (explained in Sect. 4.4) we find that 99.4% of the galaxies in the UltraVISTA-detected catalogue within the area covered by the grism spectra have a match in the 3D-HST catalogue[4]. The bottom panel of Fig. 2 shows the fraction of these galaxies that have a spectroscopic redshift or a 3D-HST grism redshift classified as robust by Momcheva et al. (2016) as a function of K_s^{tot} from UltraVISTA. Most galaxies at $K_s^{tot} \lesssim 23$ have a grism/spec-z, but this fraction drops at fainter magnitude because of a combination of the magnitude limit $[JH] < 24$ employed by Momcheva et al. (2016), using a $J + H$ band stack for detection and selection, as well as increased incompleteness at fainter magnitudes due to contamination by other objects. Nevertheless, when accounting for the K_s^{tot} distribution of our HAWK-I data and taking lensing weights into account (see Sect. 4.8), we find that effectively $\simeq 71\%$ of the relevant galaxies in the 3D-HST grism area have a robust grism/spec-z. For comparison, the corresponding fraction amounts to only 21% for optically selected weak lensing source galaxies as employed in S17, with shape measurements from ACS F606W data of single-orbit depth and a full-depth $V_{606} - I_{814}$ colour selection. Given the much higher fraction of grism/spec-z in the current study, we have to rely less on the accuracy of photometric redshift reference samples, leading to lower systematic uncertainties in the lensing analysis from the calibration of the redshift distribution (see Sect. 4.5.3). For our analysis we define a "best" redshift z_{best} from the 3D-HST catalogue, which is the spectroscopic or grism redshift of a galaxy when available, and its photometric redshift otherwise.

Skelton et al. (2014) also provide HST/WFC3-measured H-band size estimates of CANDELS galaxies, allowing us to check if the galaxy size selection applied in our HAWK-I analysis has a relevant impact on the estimation of the redshift distribution. Fig. 3 shows the distribution of the intrinsic flux radius $r_f^{int} = \sqrt{r_f^2 - r_{f,PSF}^2}$, defined via the flux radius parameter of the galaxies and stars from `SExtractor`, for the colour-selected CANDELS galaxies as a function of K_s^{tot}. This shows that $\sim 99.4\%$ of the galaxies are sufficiently resolved for shape measurements at the resolution of our HAWK-I data (limit illustrated as horizontal line in Fig. 3). As a result, the application of the size selection has a negligible impact on the estimated average geometric lensing efficiency. However, we stress that many of the galaxies are only slightly more extended than required for the shape analysis (see Fig. 3). We therefore recommend that future similar programmes do not relax the seeing requirements compared to our study, in order to not suffer from a reduced weak lensing source density.

4.3.3. Redshift comparison

We compare the 3D-HST z_{best} redshifts to the peak photometric redshifts z_p from the UltraVISTA-detected catalogue in Fig. 4. While most galaxies closely follow the one-to-one relation[5], there are some noticeable systematic features visible. Here we

[4] The non-matching galaxies can be explained through differences in the deblending and have no relevant impact on our analysis.

[5] When defining catastrophic redshift outliers as $\Delta z = |z_{best} - z_p| > 1$, 5.5% of the colour-selected galaxies shown in Fig. 4 are catastrophic redshift outliers. Excluding these catastrophic outliers, the redshift scat-

focus on those galaxies that pass our colour selection shown in black. In particular, galaxies close to the one-to-one relation with $1.4 \lesssim z_{\rm best} \lesssim 2.2$ appear to have a peak photometric redshift $z_{\rm p}$ in the UltraVISTA-detected catalogue that is slightly biased high on average. For galaxies with $2.2 \lesssim z_{\rm best} \lesssim 3.4$ this bias disappears for the galaxies close to the one-to-one relation, but there is a noticeable fraction of outliers with a $z_{\rm p}$ biased low, in some cases catastrophically with $z_{\rm p} \lesssim 0.4$. Given that these biases are in opposite directions, their impact partially cancels when computing the average geometric lensing efficiency (see Sect. 4.5).

Indications for similar outliers have already been noted by Schrabback et al. (2010) and S17. In particular, S17 compare 3D-HST photo-z to extremely deep photometric and grism redshifts available in the HUDF. While S17 conclude that the 3D-HST photo-zs are biased low in this case, this is not in contradiction with our results given that the S17 analysis is based on blue optically selected samples, which are on average significantly fainter in the NIR compared to the galaxies studied here. We interpret the different results such that a noticeable fraction of catastrophic redshift outliers, in the form of high-z galaxies incorrectly assigned a low photo-z, can be present even if NIR photometry is available, unless that has a high signal-to-noise ratio. We expect that accounting for this effect will also be relevant when calibrating redshift distributions for wide-area weak lensing surveys, e.g. employing the approach from Masters et al. (2017). As the catastrophic outliers lead to a bimodality of the colour-redshift relation, highly complete spectroscopic redshift measurements will be needed in the relevant parts of colour-colour space to adequately map out this bimodality.

4.4. Colour selection

The left panel of Fig. 5 shows the distribution of resolved galaxies with $21 < K_{\rm s}^{\rm tot} < 24.2$ within the CANDELS/COSMOS 3D-HST grism area in $g-z$ versus $z-K_{\rm s}$ colour space, with different symbols indicating different ranges in $z_{\rm best}$. The solid lines indicate our colour selection scheme, where we select background galaxies that have

$$z - K_{\rm s} > \min[g - z, 2.5]\,. \tag{14}$$

This selection is similar to the $BzK_{\rm s}$ selection introduced by Daddi et al. (2004), but slightly more conservative for the exclusion of galaxies around the cluster redshift. It is highly effective in selecting most of the background galaxies at $z_{\rm best} > 1.4$, while efficiently removing galaxies at $z_{\rm best} < 1.1$ (see Fig. 6). In particular, 98.1% of the colour-selected galaxies are in the background at $z_{\rm best} > 1.1$. At the same time, 98.9% of the galaxies in the parent catalogue at relevant cluster redshifts $0.6 < z_{\rm best} < 1.1$ are removed by this colour selection, providing an efficient suppression of cluster member contamination.

The right panel of Fig. 5 shows the distribution of galaxies in our HAWK-I+LBC shear catalogue in $g-z$ versus $z-K_{\rm s}$ colour space prior to the colour selection. In addition to the galaxy populations visible in the UltraVISTA-detected catalogue, this prominently displays the population of cluster red-sequence galaxies around $g-z \simeq 3$ and $z-K_{\rm s} \simeq 1$.

ter of the remaining galaxies can be quantified via the root mean square r.m.s.$(\Delta z/[1+z_{\rm best}]) = 0.07$.

4.5. Average geometric lensing efficiency

4.5.1. Best estimate

For the mass measurements we need to estimate the weighted-average geometric lensing efficiency (see Eq. 4) of our source sample. We start with the colour- and size-selected galaxies in the 3D-HST grism area and compute $\langle\beta\rangle_i$ from the 3D-HST $z_{\rm best}$ redshifts in magnitude bins of width 0.4 mag within $21 < K_{\rm s}^{\rm tot} < 24.2$, taking the $K_{\rm s}^{\rm tot}$-dependent shape weights into account (see Sect. 4.8). We then compute a joint estimate $\langle\beta\rangle_{\rm 3D-HST}^{\rm grism-area} = \left(\sum_i \langle\beta\rangle_i \sum_{j(i)} w_j\right) / \left(\sum_i \sum_{j(i)} w_j\right) = 0.501$ according to the shape weights w_j of the galaxies in magnitude bin i in our HAWK-I catalogue. This procedure accounts for the greater incompleteness of the HAWK-I catalogue given the lensing S/N cut.

We quantify and minimise the impact of sampling variance using the UltraVISTA-detected catalogue. For this we employ the same colour selection and weighting scheme as for the 3D-HST catalogue, but now using the peak photometric redshift $z_{\rm p}$ and dropping the size selection due to the lack of HST NIR-measured sizes in COSMOS outside the CANDELS footprint. We then compute estimates both for the full UltraVISTA ultra-deep area ($\langle\beta\rangle_{\rm UltraVISTA}^{\rm full} = 0.470$) and the 3D-HST grism area ($\langle\beta\rangle_{\rm UltraVISTA}^{\rm grism-area} = 0.490$). The latter covers the same area that was used for the analysis employing the 3D-HST $z_{\rm best}$ redshifts. Accordingly, the ratio $r_{\rm sys} = \langle\beta\rangle_{\rm UltraVISTA}^{\rm grism-area} / \langle\beta\rangle_{\rm 3D-HST}^{\rm grism-area} = 0.978$ provides us with a correction factor $r_{\rm sys}^{-1}$ to account for the impact of the systematic redshift errors in the UltraVISTA-detected catalogue discussed in Sect. 4.3.3. This can be combined with the estimate from the full UltraVISTA ultra-deep area, which suffers less from sampling variance, to obtain our best estimate of the cosmic mean geometric lensing efficiency given our selection criteria of $\langle\beta\rangle_{\rm cor} = \langle\beta\rangle_{\rm UltraVISTA}^{\rm full} / r_{\rm sys} = 0.481$.

4.5.2. Line-of-sight variations and $\langle\beta^2\rangle$

The redshift distribution within the sky patch covered by our HAWK-I observation will deviate from the cosmic mean distribution because of sampling variance. To obtain an estimate for this effect we placed 12 tiles of the same area widely distributed over the area of the UltraVISTA ultra-deep stripes. From the variation between the $\langle\beta\rangle$ estimates computed from these tiles we estimate a relative uncertainty of $\Delta\langle\beta\rangle/\langle\beta\rangle = 2.2\%$ for our analysis (for a single cluster[6]) arising from line-of-sight variations in the redshift distribution.

We account for impact of the finite width of the source redshift distribution in the lensing analysis following Hoekstra et al. (2000), for which we also require an estimate of the weighted $\langle\beta^2\rangle = 0.237$, which we compute based on the 3D-HST $z_{\rm best}$ redshifts (given the $z_{\rm p}$ outliers), but rescale with the factor $\left(\langle\beta\rangle_{\rm UltraVISTA}^{\rm full} / \langle\beta\rangle_{\rm UltraVISTA}^{\rm grism-area}\right)^2$ to account for the impact of sampling variance.

[6] A potential future scaling relation analysis that incorporates observations from a large number of clusters would have a systematic uncertainty arising from line-of-sight variations in the redshift distribution that is approximately reduced by a factor $1/\sqrt{12} \simeq 0.29$, assuming large-scale structure at high redshifts is sufficiently uncorrelated between the 12 tiles.

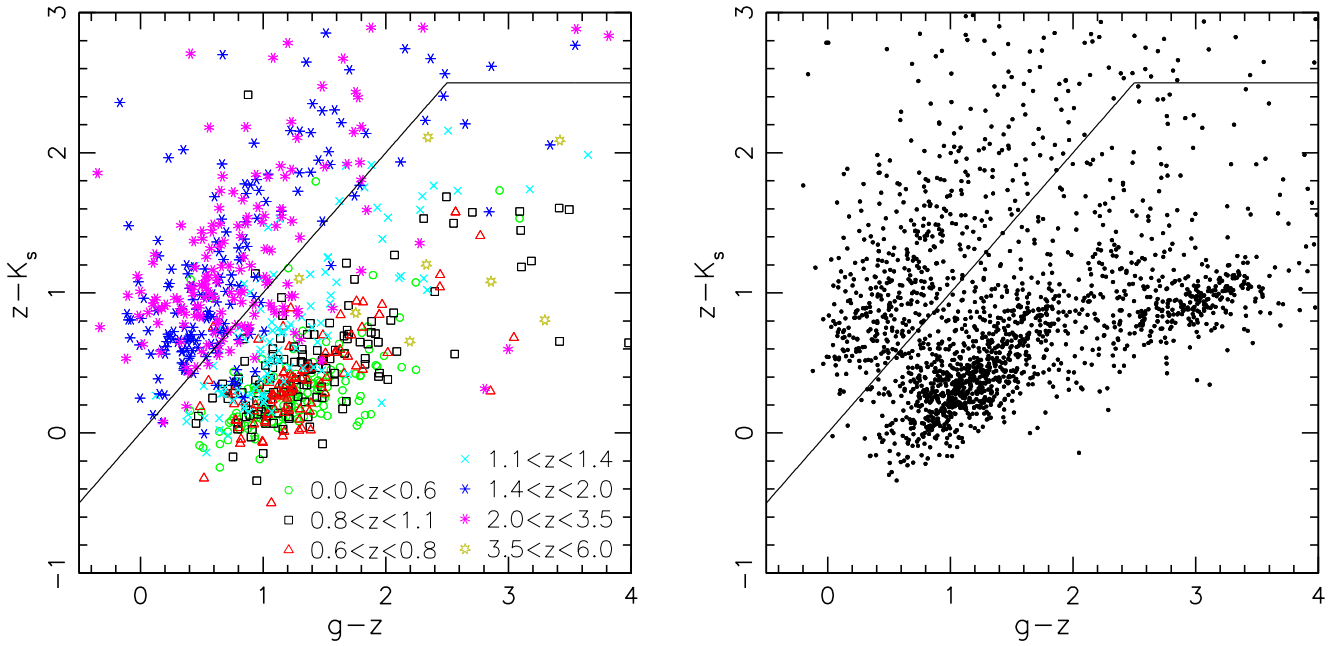

Fig. 5. Distribution of galaxies which have $21 < K_s^{tot} < 24.2$ and pass our size selection in $g-z$ vs. $z-K_s$ colour space. The black line indicates the colour selection $z-K_s > \min[g-z, 2.5]$ employed in our analysis. The *left* panel shows a random 50% fraction of the galaxies in the CANDELS/COSMOS 3D-HST grism area, with colours and symbols indicating different ranges in the best redshift estimate from 3D-HST. The *right* panel shows the galaxies passing the shape selection in our catalogue for RCS2 J2327. The excess of galaxies around $g-z \simeq 3$ and $z-K_s \simeq 1$ corresponds to the cluster red-sequence, which is efficiently removed from our background sample, along with bluer cluster members located near $g-z \simeq 1.2$ and $z-K_s \simeq 0.3$.

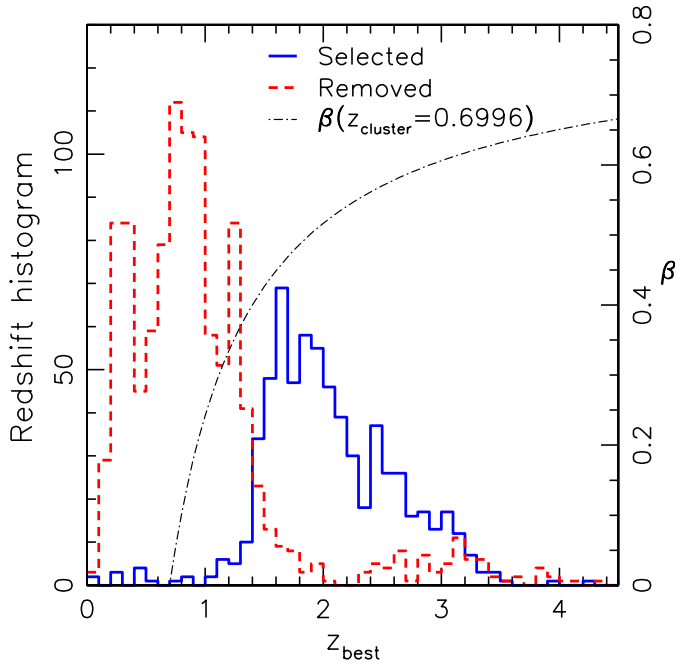

Fig. 6. Histogram of the best 3D-HST redshift estimate for sufficiently resolved galaxies with $21 < K_s^{tot} < 24.2$ within the CANDELS/COSMOS 3D-HST grism area, split between galaxies selected and removed by our gzK_s selection. The dashed-dotted curve shows the geometric lensing efficiency β as a function of source redshift.

4.5.3. Systematic uncertainties

The 3D-HST-derived $\langle\beta\rangle$ estimates are expected to be highly robust, as they are mostly based on accurate grism or spectroscopic redshifts (to $\sim 71\%$ when accounting for our weighting scheme, see Sect. 4.3.2). However, we cannot fully exclude the possibility that the $\sim 29\%$ contribution from 3D-HST photo-z may introduce systematic uncertainties because of photo-z biases. To obtain an approximate estimate for this uncertainty we recompute $\langle\beta\rangle_{3D-HST}^{grism-area}$ using the 3D-HST photometric redshifts for all galaxies (hence using 100% photo-z information instead of 29%). This leads to a very small relative increase in $\langle\beta\rangle$ by 0.4%. The expected systematic uncertainty associated with the use of $\sim 29\%$ photo-z uncertainty would on the one hand be lower than this number given the smaller fraction of employed photo-zs, but on the other hand be larger given that these galaxies are typically fainter. Considering both aspects we expect that 0.4% likely corresponds to a reasonably realistic estimate of the resulting residual uncertainty.

Additional systematic biases in $\langle\beta\rangle$ may arise from mismatches in the photometric calibration or the matching of noise properties. To quantify the impact of the former, we test the sensitivity to systematic errors in the colour measurements. We find that a systematic error in $g-z$ or $z-K_s$ colour of 0.1 mag, which provides a conservative estimate for the uncertainty in the colour calibration, leads to a relative bias in $\langle\beta\rangle$ of 0.5% only.

The matching of noise properties is complicated by the fact that our HAWK-I+LBC observations are slightly shallower in the K_s band than the reference catalogue, but deeper in the z band (see Sect. 4.3.1). Hence, we cannot simply add noise to the colours in the reference catalogue as done for K_s^{tot}. However, since the colour selection already achieves an excellent selection of background galaxies at the depth of the UltraVISTA-detected

catalogue (Fig. 6), we expect that this will also be the case for colour estimates with slightly higher signal-to-noise ratio. In order to roughly estimate the sensitivity of our analysis to noise in the colour measurements, we randomly add Gaussian scatter corresponding to a depth difference of 0.3 mag separately to the g, z, and K_s fluxes of the UltraVISTA-detected catalogue, finding that this leads to relative changes in $\langle\beta\rangle$ of +0.0%, −0.2%, and −0.1%, respectively. Biases at these levels are completely negligible compared to the statistical uncertainties of our study. Added in quadrature, the systematic errors for the $\langle\beta\rangle$ estimate identified in this subsection amount to 0.7%.

4.6. Choice of centre

For our weak lensing shear profile analysis we have to adopt a centre. This should match the position of the centre of the projected mass distribution as best as possible to minimise miscentring uncertainties (see e.g. Schrabback et al. 2017). For RCS2 J2327 the centre of the inner projected mass distribution is very well constrained by strong gravitational lensing to a location $1\farcs17^{+0\farcs47}_{-0\farcs24}$ East and $7\farcs42^{+1\farcs42}_{-0\farcs63}$ North from the Brightest Cluster Galaxy (BCG), in the direction towards the second brightest cluster galaxy (Sharon et al. 2015). This very small positional uncertainty is completely negligible for weak lensing studies (e.g. compare to von der Linden et al. 2014). We therefore fix the centre position for our analysis to the best fitting centre position of the strong lensing analysis from Sharon et al. (2015) at $(\alpha, \delta) = (351.865351, -2.074863)$ deg.

4.7. Number density profile

As shown in Sect. 4.4 our colour selection is expected to lead to a negligible residual contamination by cluster galaxies in the source sample. As a consistency check for this we investigate the radial source number density profile. Due to the central concentration of cluster galaxies a substantial residual contamination would be detectable as an increase in the source density towards the centre. For our catalogue we do not detect such a central increase. As shown in Fig. 7, the source density profile is approximately flat for radii $r \gtrsim 0.6$ Mpc, with a global mean density of 9.8 arcmin^{-2}.

Further into the cluster core the observed source density drops (see Fig. 7). We suspect that this may be due to a combination of two effects: first, we cannot detect faint background galaxies behind or close to a bright foreground cluster galaxy. In order to account for this effect at least approximately, we use a bright objects mask for the sky area calculation (already taken into account in Fig. 7, causing a $\sim 7\%$ correction in the inner bins together with the manual masks). We create this by running `SExtractor` with a high object detection threshold of 200 pixels exceeding the background by 1.5σ, and then use the "objects" check image as a mask. However, as this mask neither accounts for fainter cluster members, nor the outer wings of galaxy light profiles or the impact of intra-cluster light, it likely still leads to an underestimation of the inner source density.

Second, we suspect that lensing magnification may also lead to a net depletion in the density of faint sources. This has the largest impact in the stronger magnification regime of cluster cores (see e.g. Fort et al. 1997). Assuming source counts described by a power law and sources at a single redshift, magnification leads to a net depletion in the source counts if the slope

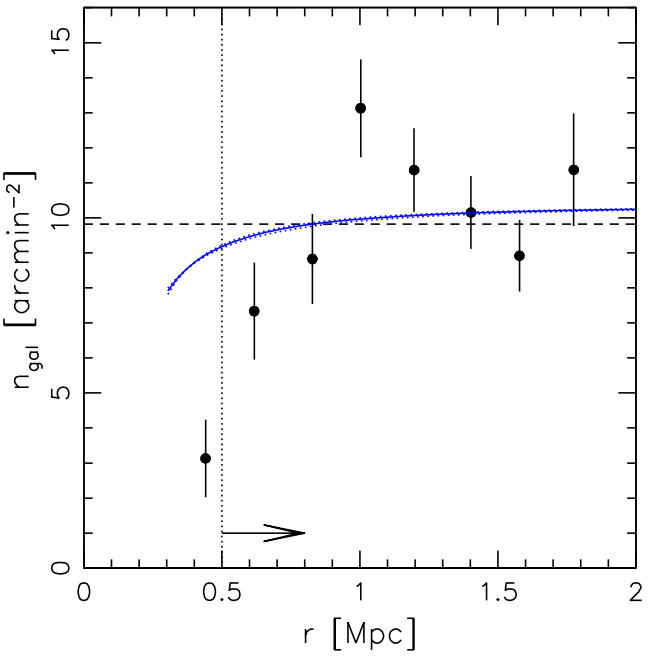

Fig. 7. Source density in our colour- and magnitude-selected weak lensing source catalogue for RCS2 J2327 as a function of projected distance from the cluster centre, taking field boundaries, manual masks, and a bright objects mask into account. Error-bars are underestimated, as they assume Poisson galaxy counts ignoring spatial clustering. The dashed black line indicates the average density over the whole field-of-view, while the blue curves indicate the approximately expected profile due to lensing magnification assuming the best-fitting NFW model for $c_{200c} = 5.1$ (solid) or $c_{200c} \in [4.1, 6.1]$ (dotted, close to the solid curve). The vertical black dotted line and the arrow indicate the lower radial limit in the weak lensing shear profile fit.

of the logarithmic cumulative number counts is shallow

$$s = \frac{\mathrm{d}\log_{10} N(<m)}{\mathrm{d}m} < 0.4 \tag{15}$$

(e.g. Broadhurst et al. 1995; Mayen & Soucail 2000). We compute this slope for the colour-selected UltraVISTA-detected catalogue around $m = K_s^{\mathrm{tot}} \simeq 24$ mag yielding $s = 0.32 \pm 0.02$ (assuming negligible incompleteness), which is indeed consistent with an expected depletion. Making the same simplifying assumptions we plot the expected source density profile resulting from magnification as solid blue curve in Fig. 7, employing the best-fit NFW density profile from our reduced shear profile fit (see Sect. 5.2). This indicates that magnification alone likely cannot explain the very low source density at $r \simeq 0.45$ Mpc, but that additional effects, such as the limitations in the bright objects mask may dominate. In addition, it may just be that the line-of-sight behind the core of RCS2 J2327 is noticeably underdense. In this respect note that the error-bars shown in Fig. 7 assume Poisson source counts but ignore spatial clustering, which underestimates the true uncertainty, and therefore overestimates the significance of the data point, as especially relevant at small radii.

4.8. Shape noise & shape weights

At fixed redshift, fainter sources tend to result in more noisy shear estimates than bright ones, for two reasons. First, the higher measurement noise leads to more noisy ellipticity mea-

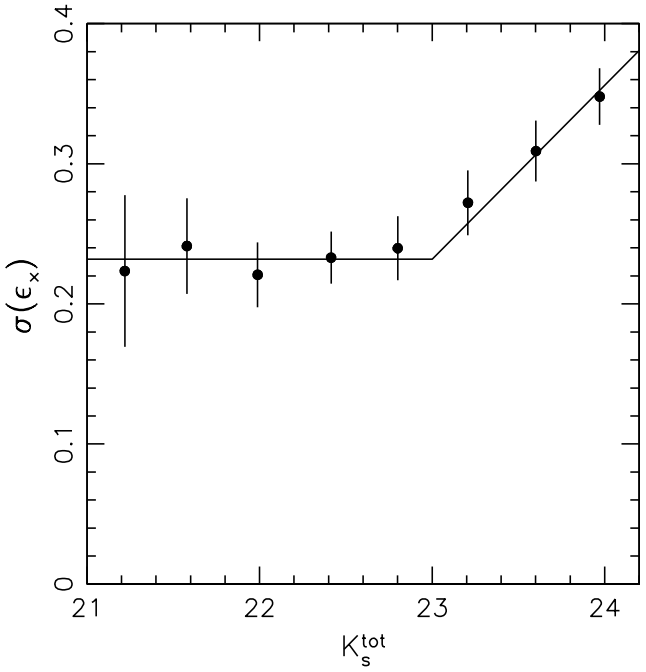

Fig. 8. Dispersion of the cross-ellipticity component with respect to the cluster centre computed in bins of K_s^{tot} including all lensing and colour-selected galaxies with a projected separation $r > 700$ kpc from the cluster centre. The solid line shows our approximate fit that is used to define shape weights.

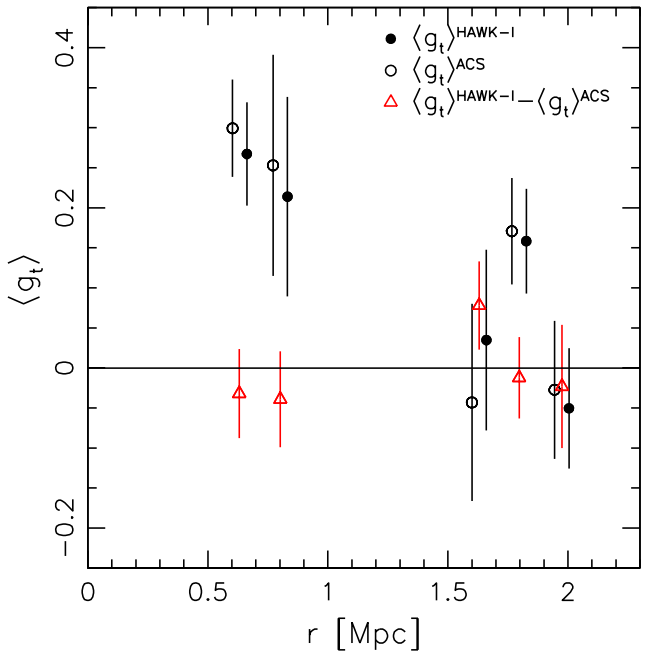

Fig. 9. Profile of the estimated tangential reduced shear for RCS2 J2327, based on the matched HAWK-I and ACS ellipticity catalogue, employing the HAWK-I+LBC colour selection and uniform weights. We display all radial bins containing at least five galaxies. The solid (open) points are based on the HAWK-I (ACS) ellipticity measurements, shown with an offset of +30 kpc (−30 kpc) for clarity. The red open triangles display the difference between the two estimates, with error-bars determined by bootstrapping the sample. Matched data are only available in the central ACS pointing and near the corners of the HAWK-I field-of-view. The resulting smaller area and lower source density leads to more noisy data compared to the analysis of the full HAWK-I+LBC-based catalogue (compare Fig. 12), and introduces the gap at intermediate radii.

surements. Second, as shown by S17, in optically selected samples the dispersion of the *intrinsic* source ellipticity increases at faint magnitudes, further increasing the noise in the shear estimate. As we show below and discuss in Sect. 6, the K_s imaging yields shape estimates for high-z galaxies with a lower measured ellipticity dispersion, indicating a lower intrinsic ellipticity dispersion than for optical high-z samples.

To account for the more noisy shear estimates at faint magnitudes, S17 employ an empirical weighting scheme according to the ellipticity dispersion measured in non-cluster fields as a function of magnitude. Given the presence of a massive cluster, that significantly shears the background galaxy images, we cannot directly apply the same approach here. However, as the cluster lensing signature primarily affects the tangential ellipticity component ϵ_t with respect to the cluster centre, but not the cross-component $\epsilon_\times$, we can use the measured dispersion of the cross-ellipticity component $\sigma_{\epsilon,\times} = \sigma(\epsilon_\times)$ as a function of K_s^{tot} (shown in Fig. 8) to define the weighting scheme. We find that $\sigma_{\epsilon,\times}(K_s^{tot})$ is approximately flat for $K_s^{tot} < 23$ with

$$\sigma_{\epsilon,0} \equiv \sigma_{\epsilon,\times}\left(21 < K_s^{tot} < 23\right) = 0.232 \pm 0.011 \quad (16)$$

and increases approximately linearly as

$$\sigma_{\epsilon,\times}\left(K_s^{tot}\right) = \sigma_{\epsilon,0} + (0.124 \pm 0.009)\left(K_s^{tot} - 23\right) \quad \text{for } K_s^{tot} > 23\,. \quad (17)$$

We expect that this increase is mostly caused by measurement noise, but we cannot exclude a possible contribution from an increase in the intrinsic ellipticity dispersion at faint magnitudes. We use $w\,(K_s^{tot}) = \sigma_{\epsilon,\times}^{-2}\,(K_s^{tot})$ as shape weight.

The K_s-measured ellipticity dispersion is significantly lower than what has been found by S17 for galaxies at similar redshifts with a largely identical shape measurement pipeline analysing optical HST/ACS images of approximately single-orbit depth. At a relatively bright magnitude $V_{606,auto} = 25$, where the contribution from measurement noise is small, S17 estimate $\sigma_\epsilon = 0.306$ for a $V_{606} - I_{814} < 0.3$ colour-selected sample. This is significantly larger than the K_s-measured σ_ϵ at bright magnitudes (Eq. 16).

4.9. Comparison to HST/ACS weak lensing shear estimates

To cross-check our HAWK-I shear estimates we compare these to measurements from overlapping HST/ACS observations (see Sect. 3.3). For the ACS catalogue generation we employ the same basic KSB+ implementation as for the HAWK-I shape measurements (see Sect. 4.1), but additionally include the principal component PSF interpolation from Schrabback et al. (2010) (building up on Jarvis & Jain 2004), as well as the PSF model calibration and shape weighting scheme from S17. For the central ACS pointing the weak lensing catalogue generation has also been described in Hoag et al. (2015).

When comparing shape measurements obtained with different resolution and/or in different band passes, a direct comparison of ellipticity estimates is not an adequate metric, as the spatial distribution of the light emission may not be identical and different effective radial weight functions are used. This is underlined by the indications we find for a significantly lower intrinsic ellipticity dispersion for the analysis based on K_s imaging com-

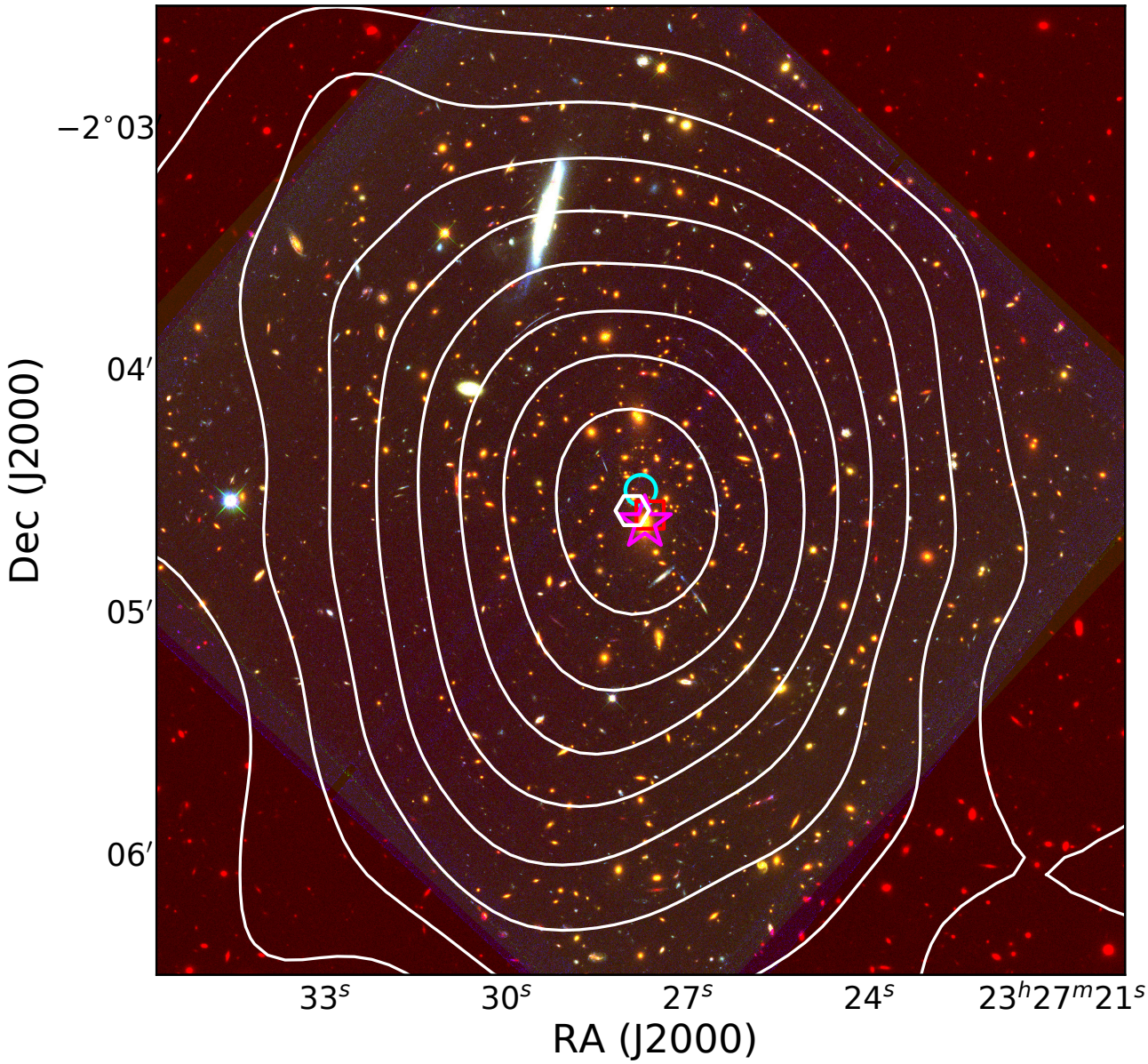

Fig. 10. RGB colour image of the central $4' \times 4'$ of RCS2 J2327 created from the VLT/HAWK-I K_s best-seeing stack and the HST/ACS F814W and F435W images. The contours indicate the weak lensing convergence reconstruction starting at $\kappa_0 = 0.04$ in steps of $\Delta\kappa = 0.04$, with the peak indicated by the white hexagon. The magenta star, red square, and cyan circle indicate the locations of the BCG, the peak in the X-ray emission, and the strong lensing centre from Sharon et al. (2015), respectively.

pared to ACS optical imaging (see Sect. 4.8). Nevertheless, what should be consistent is the estimated reduced tangential cluster shear profile when a matched catalogue with identical weights is used. This is shown in Fig. 9, where we employ the HAWK-I+LBC colour selection and uniform weights for the galaxies in the matched HAWK-I and ACS ellipticity catalogue. As the difference in the reduced shear estimates $\langle g_t \rangle^{\mathrm{HAWK-I}} - \langle g_t \rangle^{\mathrm{ACS}}$ is consistent with zero, we conclude that the HAWK-I and ACS measurements are fully consistent within the current statistical uncertainty.

5. Cluster weak lensing results

5.1. Mass reconstruction

We reconstruct the convergence (κ) distribution of RCS2 J2327 on a grid, using an improved version of the Kaiser & Squires (1993) formalism, which applies a Wiener filter as described in McInnes et al. (2009) and Simon et al. (2009), and as further detailed in S17. Given the mass-sheet degeneracy we cannot constrain the average convergence in the field-of-view. We fix it to zero, which is adequate for large fields-of-view, but likely leads to an underestimation for our data. This uncertainty is however not a concern for our analysis as we use the mass reconstruction only for illustration and consistency checks regarding the location of the cluster centre. Given the high cluster mass we apply an iterative reduced-shear correction (e.g. Seitz & Schneider 1996) based on the κ distribution from the previous iteration.

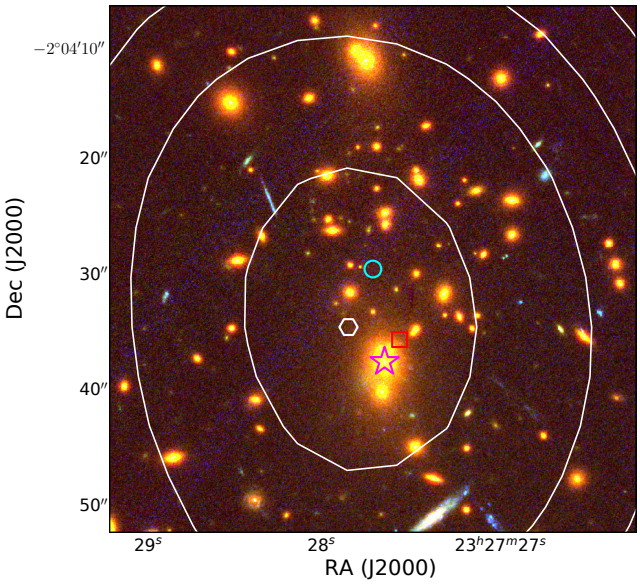

Fig. 11. As Fig. 10, but showing a cut-out of the central $45'' \times 45''$ with contours in steps of $\Delta\kappa = 0.02$, where the innermost contour corresponds to $\kappa = 0.34$.

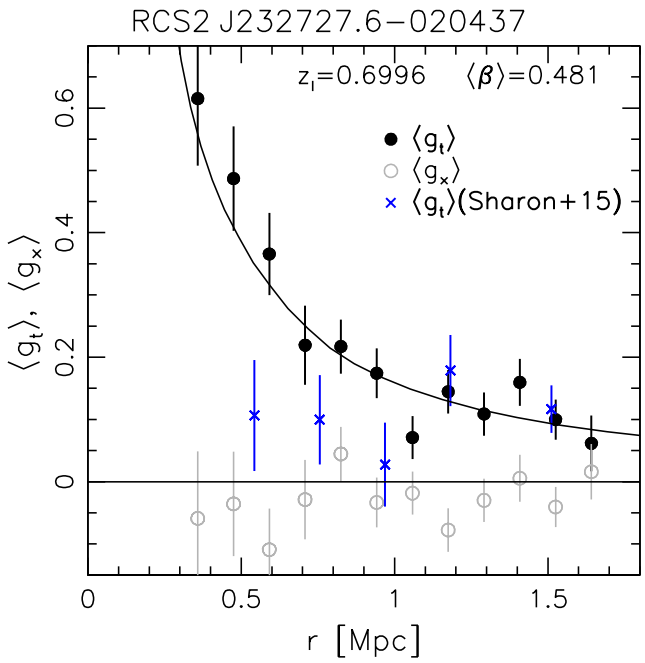

Fig. 12. Profile of the tangential reduced shear (filled circles) and the 45 degrees-rotated cross-component (open circles) for RCS2 *J*2327 as function of cluster-centric separation. The solid curve shows the best-fitting NFW model prediction for a fixed concentration $c_{200c} = 5.1$ when considering scales $500\,\mathrm{kpc} < r < 1.6\,\mathrm{Mpc}$. The blue crosses indicate tangential reduced shear estimates from Sharon et al. (2015) based on deep CFHT weak lensing measurements, scaled to the same $\langle\beta\rangle$ and excluding points at small radii that are not included in their fit. Sharon et al. (2015) also incorporate measurements at larger radii which are not shown here.

Fig. 10 shows contours of the resulting reconstruction starting at $\kappa_0 = 0.04$ in steps of $\Delta\kappa = 0.04$, with a peak value $\kappa_{\max} = 0.347$.

To estimate the peak significance we apply the same reconstruction algorithm to noise catalogues generated by randomising the ellipticity phases. Dividing the reconstruction from the real data through the r.m.s. image of the noise reconstructions we estimate a 10.1σ peak significance. In Fig. 10 the contours are overlaid on an RGB colour image based on the HAWK-I K_s and the ACS F814W and F435W images, with indications of the BCG, as well as the strong lensing centre and the peak of the X-ray emission from Sharon et al. (2015). The peak of the weak lensing κ-reconstruction at $(\alpha, \delta)_{\mathrm{peak}} = (351.86594, -2.07626)$ deg is constrained to $(\Delta\alpha, \Delta\delta)_{\mathrm{peak}} = (3\farcs2, 5\farcs7)$ as estimated by bootstrapping the source catalogue, making it consistent with the locations of the BCG, X-ray centre, and strong lensing centre (see also Fig. 11) within $\sim 1\sigma$.

5.2. Reduced shear profile analysis and mass constraints

Weak lensing measurements can provide non-parametric estimates of projected cluster masses via the aperture mass statistic (e.g. Hoekstra et al. 2015) if the lensing signal is measured well beyond the cluster virial radius. As the HAWK-I field of view does not provide such a large radial coverage for RCS2 *J*2327, we instead have to rely on model fits of the cluster tangential reduced shear profile in order to constrain the cluster mass. This effectively breaks the mass-sheet degeneracy discussed in Sect. 5.1. In practise such idealised mass sheets are related to correlated and uncorrelated large-scale structure projections. The net impact of such projections for weak lensing mass estimates is additional scatter, as computed and discussed below.

We show the tangential reduced shear profile of RCS2 *J*2327 as a function of separation from the strong lensing centre[7] (see Sect. 4.6) as estimated from our HAWK-I+LBT catalogue in Fig. 12. We fit these data using reduced shear profile predictions from Wright & Brainerd (2000) assuming a spherical NFW density profile (Navarro et al. 1997). Here we only consider radii in the range $500\,\mathrm{kpc} < r < 1.6\,\mathrm{Mpc}$. At smaller radii the measured tangential reduced shear exceeds the regime tested in the weak lensing image simulations (see Sect. 4.1). At larger scales the azimuthal coverage gets increasingly incomplete.

The weak lensing data alone cannot constrain the cluster concentration c_{200c} sufficiently well, which is why we revert to results from numerical simulations. Using a suit of simulations, Diemer & Kravtsov (2015) provide a well-calibrated prescription to compute the expected mean halo concentration as a function of mass, which would be adequate for a general cluster. However, the X-ray analysis from Sharon et al. (2015) indicates that RCS2 *J*2327 is a fairly relaxed cluster, which is why, on average, a higher concentration should be expected than for a general cluster. Neto et al. (2007) investigate the difference in structural parameters for relaxed versus general simulated dark matter haloes at redshift $z = 0$. They find that haloes at the mass-scale of RCS2 *J*2327 have on average larger median concentrations compared to general haloes by a factor 1.16. Assuming that this factor also holds at higher redshifts, we conduct a two-step fit for RCS2 *J*2327: first, we fit the data assuming the concentration–mass relation from Diemer & Kravtsov (2015), yielding a best-fit cluster mass which corresponds to a mean $c_{200c,D15} = 4.4$. Based on the results from Neto et al. (2007) we then repeat the fit assuming a larger concentration $c_{200c} = 1.16\, c_{200c,D15} = 5.1$ yield-

[7] We do not centre on the peak of the weak lensing mass reconstruction from Sect. 5.1 as this is expected to yield mass constraints that are biased high (e.g. Dietrich et al. 2012). However, this would likely be a minor effect given our very high-significance detection.

ing

$$M_{200c}/(10^{15}\mathrm{M}_\odot) = 2.06^{+0.28}_{-0.26}(\mathrm{stat.}) \pm 0.12(\mathrm{sys.})\,, \quad (18)$$

where the statistical error contains contributions added in quadrature from shape noise ($^{+0.21}_{-0.20} \times 10^{15}\mathrm{M}_\odot$), large-scale structure projections ($\pm 0.12 \times 10^{15}\mathrm{M}_\odot$) as estimated in S17, line-of-sight variations in the source redshift distribution ($\pm 0.07 \times 10^{15}\mathrm{M}_\odot$; see Sect. 4.5), and the impact of the uncertainty in the concentration ($^{+0.12}_{-0.10} \times 10^{15}\mathrm{M}_\odot$). We derive the latter uncertainty from the estimated scatter in the logarithm of the concentration $\sigma(\log_{10} c_{200c}) = 0.061$ for high-mass relaxed haloes as found by Neto et al. (2007). The systematic error in Eq. 18 is dominated by the shear calibration ($\pm 0.12 \times 10^{15}\mathrm{M}_\odot$; see Sect. 4.1) with a minor contribution from the systematic uncertainty of the $\langle\beta\rangle$ estimate ($\pm 0.02 \times 10^{15}\mathrm{M}_\odot$; see Sect. 4.5.3). Based on the M_{200c} limits and fixed concentration we also report mass constraints for an overdensity $\Delta = 500$ of

$$M_{500c}/(10^{15}\mathrm{M}_\odot) = 1.50^{+0.19}_{-0.17}(\mathrm{stat.}) \pm 0.09(\mathrm{sys.})\,, \quad (19)$$

taking the same sources of uncertainty into account. Note that the sensitivity to the uncertainty in the concentration is lower for M_{500c} (3% relative uncertainty) than for M_{200c} (5% relative uncertainty). While the weak lensing data cannot constrain the radii corresponding to the considered overdensities Δ separately, we list the best-fitting values $r_{200c} = 2.03$ Mpc and $r_{500c} = 1.34$ Mpc given the assumed concentration to simplify possible mass comparisons in future studies.

Note that our assumptions regarding the concentration–mass relation are also consistent with recent findings from the CLASH project (Postman et al. 2012). In particular, the constraints derived by Umetsu et al. (2016) on the concentration–mass relation of massive clusters using combined strong lensing, weak lensing, and magnification measurements are fully consistent with the Diemer & Kravtsov (2015) relation, which we use as a basis to estimate the mean concentration for a general cluster population as function of mass and redshift. Meneghetti et al. (2014) find a higher average concentration for simulated clusters with regular X-ray morphologies resembling a subset of the CLASH clusters, similar to the results from Neto et al. (2007) for relaxed haloes. While most CLASH clusters are at significantly lower redshifts compared to RCS2 J2327, limiting a direct comparison, there are two CLASH clusters with a similar or higher redshift (MACS J0744+39 and CL J1226+3332). For these clusters Merten et al. (2015) estimate concentrations $c_{200c} = 4.1 \pm 1.0$ and $c_{200c} = 4.0 \pm 0.9$, respectively, in reasonable agreement with the simulation-based priors assumed in our analysis.

For a pure lensing signal the 45 degrees-rotated cross-component, shown as the open circles in Fig. 12, should be consistent with zero. The measured signal appears to be slightly negative, with a significance at the 1.9σ level when all data points at $r > 1$ Mpc are considered. This could possibly indicate the presence of residual systematics, e.g. from incomplete PSF anisotropy correction, which is typically referred to as additive shape measurement bias. While our employed basic KSB+ implementation was among the methods with the lowest additive biases in the blind test analysis from Heymans et al. (2006), there are simplifying assumptions in the KSB+ approach that may break down for complex PSFs (e.g. Kaiser 2000). As a sensitivity test to investigate if this can have a significant impact on our analysis, we artificially doubled the level of the PSF anisotropy correction. This reduces the significance of the negative cross-component to 1.1σ, but has only a very minor +2.7% impact on the estimated cluster mass. Compared to the statistical uncertainty we conclude that possible PSF anisotropy residuals are therefore of no concern for our current study. Potential future investigations with larger samples will be able to test for possible residual systematics with a higher sensitivity. If detected, such analyses could revert to alternative shape estimation techniques, which do not rely on simplifying assumptions regarding the PSF (e.g. Melchior et al. 2011).

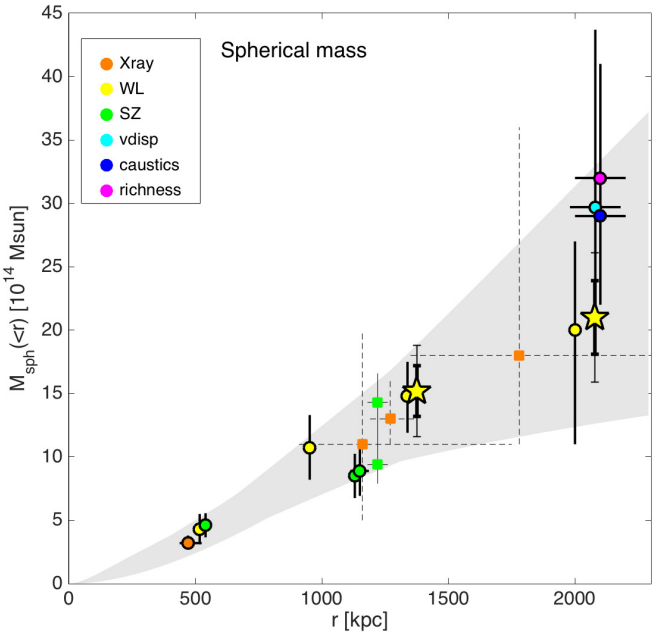

Fig. 13. Updated version of Fig. 16 from Sharon et al. (2015), showing different estimates for the enclosed spherical mass of RCS2 J2327 as function of radius. The stars-shaped data points show our weak lensing measurements, recomputed for $\Omega_m = 0.27$ and $\Omega_\Lambda = 0.73$ as assumed by Sharon et al. (2015). The think (thin) error-bars correspond to our combined statistical and systematic uncertainty without (with) including an additional ∼ 20% intrinsic scatter from cluster triaxiality and correlated large-scale structure. The green squares show SZ mass estimates from Hasselfield et al. (2013). The other mass measurements are described in Sharon et al. (2015) and were derived from Magellan spectroscopic, *Chandra* X-ray, SZA Sunyaev-Zel'dovich, and CFHT wide-field weak lensing observations, as well as richness measurements, where points with dashed error-bars indicate extrapolated results. The shaded grey region shows the 1σ range of spherical NFW mass profiles Sharon et al. (2015) fit to the spherical mass estimates marked with thick circles.

5.3. Comparison to results from previous studies

Sharon et al. (2015) present a first weak lensing analysis of RCS2 J2327 based on deep wide-field CFHT/Megacam observations, yielding a mass constraint $M_{200c} = 2.0^{+0.9}_{-0.8} \times 10^{15}\mathrm{M}_\odot$. Recomputing our analysis for the cosmology assumed in their study (ΛCDM with $\Omega_m = 0.27$, $\Omega_\Lambda = 0.73$, and $h = 0.7$) our result $M_{200c}/(10^{15}\mathrm{M}_\odot) = 2.10^{+0.29}_{-0.27}(\mathrm{stat.}) \pm 0.12(\mathrm{sys.})$ is fully consistent with this previous measurement, but provides a three times tighter constraint. The major increase in sensitivity is also visible in Fig. 12, where the estimated tangential reduced shear profiles of the two studies scaled to the same $\langle\beta\rangle$ are compared. While the CFHT results are noisier, they agree well for scales 1 Mpc $\lesssim r \lesssim$ 1.7 Mpc. However, at smaller radii the re-scaled estimate from Sharon et al. (2015) is significantly lower than our estimated reduced shear profile. This may be a consequence of

the colour selection scheme employed in Sharon et al. (2015), which yields only a partial removal of cluster galaxies and therefore needs to be complemented with a contamination correction, thereby introducing additional uncertainties especially at smaller radii. Note that Sharon et al. (2015) also include measurements at larger radii, which are not probed by our HAWK-I observations.

We can also compare our weak lensing cluster mass constraints with mass estimates derived by Sharon et al. (2015) and Hasselfield et al. (2013) using other techniques. In particular, we compare to SZ and dynamical mass estimates, as they probe the cluster mass distribution at similar scales as the weak lensing signal. The dynamical mass constraints tend to be higher, e.g. $M_{200c}/(10^{15}\mathrm{M}_\odot) = 2.9^{+1.0}_{-0.7}$ from a caustics analysis, but are still consistent with our measurements. There is a noticeable spread in the SZ-derived mass constraints for the cluster. Sharon et al. (2015) estimate a mass $M_{500c}/(10^{15}\mathrm{M}_\odot) = 0.85 \pm 0.11$ based on scaling relations from Andersson et al. (2011) or $M_{500c}/(10^{15}\mathrm{M}_\odot) = 0.89 \pm 0.08$ when employing the method from Mroczkowski (2011). Hasselfield et al. (2013) obtain a similar mass estimate $M_{500c}/(10^{15}\mathrm{M}_\odot) = 0.94 \pm 0.15$ when assuming universal pressure profiles, but higher masses when assuming other scaling relations or models, e.g. $M_{500c}/(10^{15}\mathrm{M}_\odot) = 1.49 \pm 0.30$ based on dynamical masses from Sifón et al. (2013). Our derived constraint $M_{500c}/(10^{15}\mathrm{M}_\odot) = 1.52^{+0.19}_{-0.17}(\mathrm{stat.}) \pm 0.09(\mathrm{sys.})$ (when assuming the same cosmology as Sharon et al. 2015) agrees well with the latter SZ results. Note that our mass constraint assumes a spherical NFW mass model. Cluster triaxiality and correlated large-scale structure can introduce an additional $\simeq 20\%$ intrinsic scatter in comparison to the 3D halo mass (compare e.g. Becker & Kravtsov 2011). Likewise, there is intrinsic scatter between the 3D halo mass and SZ-inferred mass estimates. Fig. 13 compares our results to the mass estimates from Sharon et al. (2015) and Hasselfield et al. (2013), where we show error-bars for our constraints both with and without including intrinsic scatter.

Our analysis confirms that RCS2 *J*2327 is one of the most massive clusters known in the $z \gtrsim 0.7$ Universe. Its largest rival is likely ACT-CL *J*0102−4915 (Menanteau et al. 2012), for which existing weak lensing measurements indicate a possibly higher mass, but here the uncertainties are increased because of the complex merger geometry (compare S17; Jee et al. 2014). Comparing our improved mass constraints for RCS2 *J*2327 with the analysis from Buddendiek et al. (2015) we conclude that the existence of RCS2 *J*2327 does not pose a significant challenge to standard ΛCDM predictions.

6. Weak lensing performance: HAWK-I versus ACS

A primary goal of this study is to investigate whether our experimental setup, which employs shape measurements in high-resolution ground-based K_s images and a $g-z$ versus $z-K_\mathrm{s}$ colour selection, can provide a viable alternative to mosaic HST observations for the weak lensing analysis of massive galaxy clusters at moderately high redshifts. For this we compare our results to the study from S17, as summarised in Table 1. S17 measure shapes in 2×2 ACS F606W mosaics with single-orbit depth per pointing using the same underlying KSB+ implementation employed here. They apply a $V_{606} - I_{814} < 0.3$ colour selection (for clusters at $0.6 \lesssim z_\mathrm{l} \lesssim 1.0$). Here we consider only the case of adequately deep data for the colour selection as provided e.g. by the ACS F814W imaging in S17. While the ACS background-selected source density is higher by a factor 1.85, this advantage is almost completely cancelled by the larger $\sigma_{\epsilon,\mathrm{eff}}$ and the slightly lower $\langle\beta\rangle$ for the ACS catalogue (quoted numbers assume a cluster at $z_\mathrm{l} = 0.7$), yielding very similar weak lensing sensitivity factors f (see Eq. 8) with $f_{\mathrm{HAWK-I}}/f_{\mathrm{ACS}} = 0.95$. Hence, our HAWK-I+LBC setup provides a nearly identical weak lensing sensitivity as the ACS setup employed by S17.

An important reason for the good performance of the HAWK-I+LBC setup is given by the lower effective ellipticity dispersion $\sigma_{\epsilon,\mathrm{eff}}$ found for the colour-selected HAWK-I shear catalogue (see Sect. 4.8). In part this may be due to differences in the selected galaxy populations. But even for galaxies that would be included in both the HAWK-I and the ACS selection schemes we expect that the K_s-based shape measurements yield a lower intrinsic ellipticity dispersion as they primarily probe the smoother and typically rounder stellar component. In contrast, probing rest-frame UV wavelengths, the optical ACS imaging primarily shows clumpy star-forming regions, yielding more irregular shapes with a larger ellipticity dispersion. As illustration, we compare the HAWK-I K_s images for some of the galaxies in our weak lensing catalogue to their counter parts in ACS F814W images in Fig. 14. For example, the second but last galaxy shown in rows three and four exhibits a small light-emitting region in the ACS image likely constituting a compact star-forming region, which is spatially offset compare to the centre of the stellar light distribution visible in the K_s image.

In addition to the statistical performance we also have to compare the systematic uncertainties associated with both approaches, which is particularly relevant when considering future studies of larger samples. For this we ignore mass modelling uncertainties, as they are essentially identical for both approaches given the similar radial coverage, and given that they can be improved via simulations (e.g. see the discussion in S17). Residual shape measurement biases are in principle expected to be lower for the ACS-based analysis given the higher resolution (e.g. Massey et al. 2013). However, we expect that shape measurement biases will not be a limiting systematic for the analysis of future large weak lensing follow-up programmes of massive high-z clusters. Any such programme that is realistically conceivable in the next years will have statistical uncertainties at the several per cent level, which is why systematic error control at the $\sim 1\%$-level suffices (see also Köhlinger et al. 2015). With advanced shape measurement techniques this level of accuracy has already been demonstrated for cosmic shear measurements (e.g. Fenech Conti et al. 2017), while Bernstein et al. (2016) even achieve a further order of magnitude improvement on simplified simulations. Additionally, Hoekstra et al. (2015, 2017) demonstrate how image simulations can be employed to calibrate shape measurement techniques for the impact of real survey effects for next generation cosmic shear experiments. What is currently still missing is the calibration of shape measurement algorithms in the stronger shear regime of clusters (see e.g. LSST Dark Energy Science Collaboration 2012), but such efforts are already well underway (e.g. Hernández-Martín et al. in prep.).

This leaves the final and most relevant source of systematic uncertainty, which is the calibration of the source redshift distribution and estimation of $\langle\beta\rangle$. Combining the different relevant contributors to this uncertainty in S17, the current systematic uncertainty on $\langle\beta\rangle$ amounts to $\sim 2.6\%$ for the ACS-based analysis. For comparison, the systematic effects considered in Sect. 4.5.3 yield a smaller combined systematic uncertainty on $\langle\beta\rangle$ for the HAWK-I-based analysis of $\sim 0.7\%$. One of the reasons for this low systematic uncertainty is the availability of NIR-selected reference samples with deep high-quality redshift information. In particular in the 3D-HST reference sample effectively $\sim 71\%$ of the colour-selected galaxies at the relevant depth

Table 1. Comparison of weak lensing data and performance.

	HAWK-I+LBC analysis	S17-like ACS analysis (with full-depth colour selection)
Shapes from (total duration)	VLT/HAWK-I K_s ($\simeq 7$ h)	HST/ACS $F606W$ 2×2 mosaic (4 orbits $\simeq 6.3$ h)
For colours (total duration)	LBT/LBC $g + z$ ($\simeq 2$ h)	HST/ACS $F814W$ mosaic ($\simeq 6.3$ h) or 8m-class i band ($\simeq 2$ h)[1]
Useful field-of-view	$\simeq 7' \times 7'$	$\simeq 6\farcm5 \times 6\farcm5$
PSF FWHM	$\simeq 0\farcs35$	$\simeq 0\farcs1$
$n_{\rm gal}$/arcmin^{-2}	9.8 (for $z_l \leq 1.1$)	18.1 (for $z_l \leq 1.0$)[2]
$\langle\beta\rangle(z_l = 0.7)$	0.481	0.466
$\sigma_{\epsilon,\rm eff}$	0.259	0.322
f/arcmin$^{-1}(z_l = 0.7)$	5.82	6.15

Notes. — [1]: This corresponds to the F814W/i-band imaging that would be needed in order to apply the colour selection for the full depth of the shape catalogue, in order to reach the source density $n_{\rm gal}$.
[2]: S17 reach this average source density for a colour selection including F814W imaging and clusters at $z_l \leq 1.0$. At higher cluster redshifts a more stringent colour selection reduces the source density.

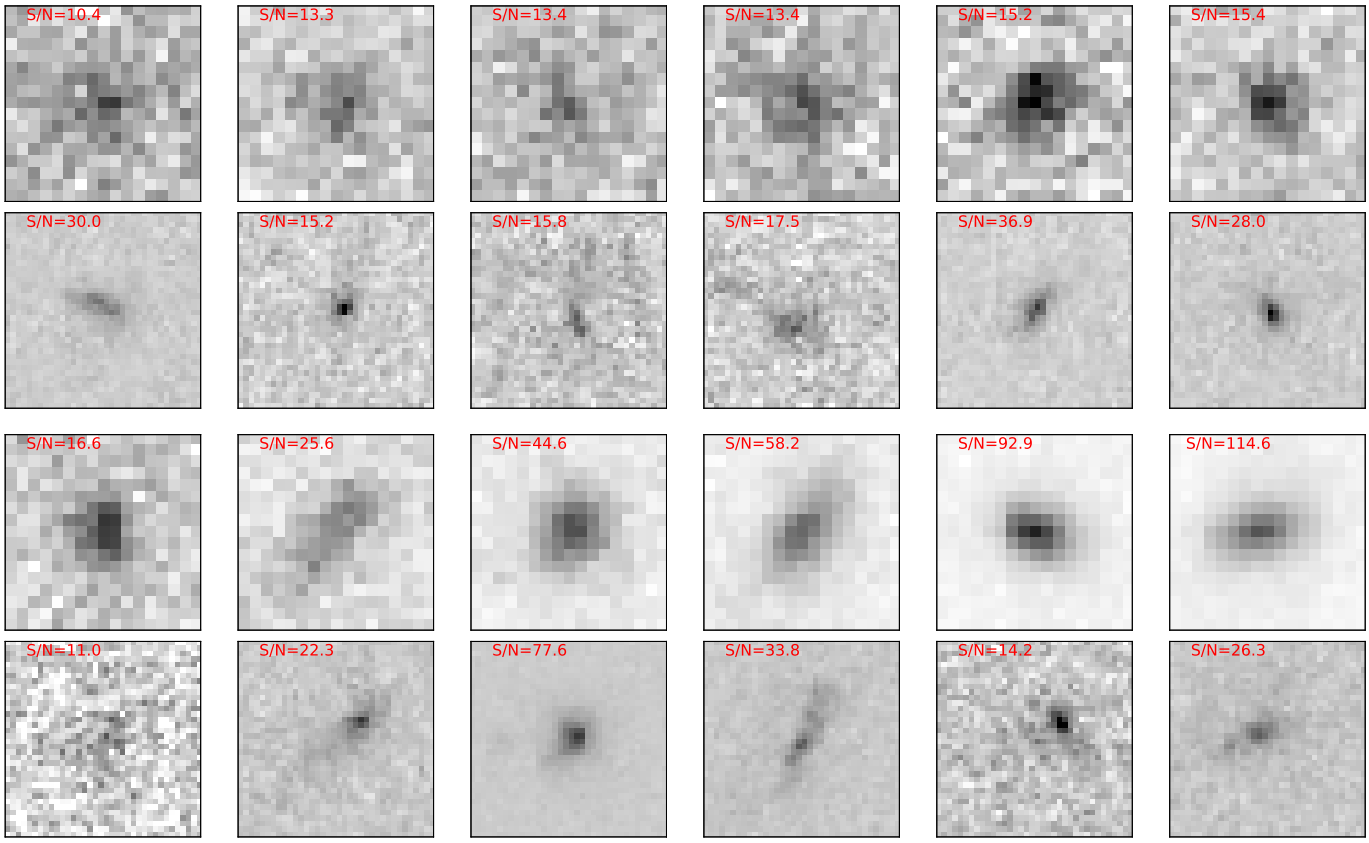

Fig. 14. $2\farcs0 \times 2\farcs0$ cut-outs of background-selected galaxies that are included in *both* the weak lensing catalogue obtained from the VLT/HAWK-I imaging *and* the weak lensing catalogue derived from the HST/ACS data. Rows one and three show the HAWK-I cut-outs sorted according to the HAWK-I $(S/N)_{\rm flux}$, while rows two and four show the corresponding ACS cut-outs of the same galaxies. All cut-outs are oriented with North=up and East=left, and are centred on the HAWK-I galaxy position. The grey scale is linear with flux for all cut-outs, but the range in flux is adjusted according the individual $(S/N)_{\rm flux}$.

have a spectroscopic or HST/WFC3 grism redshift when taking our source magnitude distribution and weights into account (see Sect. 4.3.2). Comparably deep and complete spectroscopic reference samples do not yet exists for the deep optically selected ACS weak lensing data sets (but note that samples are increasing, see e.g. Le Fèvre et al. 2015). In S17 a significant contribution to the systematic uncertainty related to the $\langle\beta\rangle$ estimate comes from the correction for catastrophic redshift outliers. These incorrectly scatter from the high-z source population into a low-z contamination sample, which cannot be removed with the colour selection scheme from S17. The gzK_s selection applied in our current study does not suffer from such a low-z contamination, and is therefore affected less by catastrophic redshift outliers.

Further advantages of the HAWK-I+LBC-based analysis are the applicability of the chosen default colour selection scheme out to a higher maximum cluster redshift $z_{\rm l,max} = 1.1$ (instead of $z_l = 1.0$ for the $V_{606} - I_{814} < 0.3$ ACS colour selection scheme), which can possibly be extended to $z_{\rm l,max} \simeq 1.2$–1.3 (instead of $z_l = 1.15$ for the ACS-based analysis) with more stringent colour selection criteria (compare Figures 5 and 6). Also, the HAWK-I+LBC-based colour selection yields a better suppres-

sion fraction of galaxies at relevant cluster redshifts (98.9% versus 98.1%).

Taking all this together we conclude that the chosen setup of the HAWK-I+LBC data yields a weak lensing performance that is similarly powerful as the considered ACS-based analysis scheme. While the required integration time is significant for the K_s imaging, this is compensated by the ability to cover a larger field-of-view with imagers like HAWK-I. The K_s-based approach is therefore particularly efficient for the analysis of high-mass ($M_{200c} > 5 \times 10^{14} M_\odot$) clusters at redshifts $0.7 \lesssim z_l \lesssim 1.1$, for which mosaics would be needed with HST/ACS to probe the weak lensing signal out to approximately the virial radius[8] (see Table 1 for the approximate total observing times). For less massive clusters and clusters at even higher redshifts deeper observations are needed, while a wide angular coverage is less important (e.g. Jee et al. 2011). In this regime deeper single pointing HST observations likely provide a more adequate observing strategy, as required K_s integration times would become prohibitively long, and the virial radius fits within the ACS field-of-view.

7. Summary and conclusions

We have presented the first weak gravitational lensing analysis that exploits the superb image resolution (FWHM* = 0.″35) that can be achieved in the K_s band under good seeing conditions with optimised imagers such as the employed VLT/HAWK-I to measure weak lensing galaxy shapes. Here we summarise our main conclusions:

- At the resolution of the K_s imaging, nearly all relevant background galaxies are sufficiently resolved for weak lensing measurements.
- The employed photometric selection in $g - z$ versus $z - K_s$ colour space is highly effective for the selection of most of the lensed background galaxies and the removal of diluting foreground and cluster galaxies.
- Our analysis indicates that the intrinsic ellipticity dispersion is noticeably lower for high-z galaxies in K_s weak lensing data compared to high-z sources studied in the optical, boosting the weak lensing sensitivity.
- Despite a lower source density the analysed data therefore yield almost the same weak lensing sensitivity as the analysis of mosaic HST/ACS data with single-orbit depth per pointing from S17.
- The systematic uncertainty regarding the calibration of the source redshift distribution is lower for the HAWK-I analysis compared to the S17 ACS analysis. This is thanks to the use of NIR-selected redshift reference samples from 3D-HST and UltraVISTA, as well as the better removal of contaminating low-z galaxies from the source sample, reducing the sensitivity to catastrophic redshift errors.
- Comparing to HST/ACS data that overlap with parts of our HAWK-I observations of RCS2 $J2327$, we find fully consistent estimates of the tangential reduced shear profile between the two data sets in a matched catalogue, providing an important confirmation for the K_s-based analysis.
- Given the larger field-of-view, good-seeing VLT/HAWK-I K_s observations, complemented with g and z (or B and z) photometry, provide an efficient alternative to mosaic HST/ACS observations for the weak lensing analysis of massive galaxy clusters at redshifts $0.7 \lesssim z_l \lesssim 1.1$.
- Especially for clusters at higher redshifts significantly deeper observations with higher resolution are required, while a smaller field-of-view is typically sufficient. In this regime deep HST observations with a smaller angular coverage provide the most effective and efficient observing strategy.
- We stress that calibrations of the source redshift distribution for weak lensing studies have to carefully account for catastrophic redshift outliers, which appear to be present even when NIR imaging is available (see Sect. 4.3.3).
- While our observations confirm that RCS2 $J2327$ is one of the most massive galaxy clusters known in the $z \gtrsim 0.7$ Universe, its existence is not in tension with standard ΛCDM expectations according to our mass constraints.
- The extreme mass of RCS2 $J2327$ leads to the significant weak lensing signal we detect, but we stress that our conclusions regarding the sensitivity of the HAWK-I weak lensing measurements (hence, the noise level) do not depend on its extreme mass. The approach is also directly applicable to massive, but less extreme clusters at redshifts $0.7 \lesssim z_l \lesssim 1.1$ (e.g. from the Bleem et al. 2015 sample).

[8] The achievable signal-to-noise ratio of the mass constraints naturally increases with cluster mass and decreases with cluster redshift. E.g., for an individual $M_{200c} \simeq 6 \times 10^{14} M_\odot$ cluster at $z \simeq 1.0$ and a setup similar to our analysis we expect a $\sim 50\%$ statistical mass uncertainty.

Acknowledgements. This work is directly based on observations collected at the European Organisation for Astronomical Research in the Southern Hemisphere under ESO programme(s) 087.A-0933, at the Large Binocular Telescope (LBT), and with the NASA/ESA Hubble Space Telescope under GO programmes 13177 and 10846. This work also makes use of catalogues created by the 3D-HST Treasury Program (GO 12177 and 12328), as well as catalogues derived from the ESO UltraVISTA Programme 179.A-2005. We thank ESO staff for obtaining the excellent VLT/HAWK-I images and Paul Martini, David Atlee, Erica Hesselbach, Jeff Blackburne, and Matthias Dietrich for conducting the LBT/LBC observations. We thank Patrick Simon for providing the codes employed in this work to reconstruct the cluster mass distribution and to generate Gaussian shear field realisations for the estimation of the impact of large-scale structure projections. We thank Peter Schneider for useful discussions and for providing comments on this manuscript. TS, DA, BH, and DK acknowledge support from the German Federal Ministry of Economics and Technology (BMWi) provided through DLR under projects 50 OR 1210, 50 OR 1308, 50 OR 1407, and 50 OR 1610. RFJvdB acknowledges support from the European Research Council under FP7 grant number 340519. TE is supported by the Deutsche Forschungsgemeinschaft in the framework of the TR33 'The Dark Universe'. HHi is supported by an Emmy Noether grant (No. Hi 1495/2-1) of the Deutsche Forschungsgemeinschaft. This work was supported in part by the Kavli Institute for Cosmological Physics at the University of Chicago through grant NSF PHY-1125897 and an endowment from the Kavli Foundation and its founder Fred Kavli. HST is operated by the Association of Universities for Research in Astronomy, Incorporated, under NASA contract NAS5-26555. The LBT is an international collaboration among institutions in the United States, Italy and Germany. LBT Corporation partners are: The University of Arizona on behalf of the Arizona university system; Istituto Nazionale di Astrofisica, Italy; LBT Beteiligungsgesellschaft, Germany, representing the Max-Planck Society, the Astrophysical Institute Potsdam, and Heidelberg University; The Ohio State University, and The Research Corporation, on behalf of The University of Notre Dame, University of Minnesota and University of Virginia. This research made use of APLpy, an open-source plotting package for Python (Robitaille & Bressert 2012).

References

Andersson, K., Benson, B. A., Ade, P. A. R., et al. 2011, ApJ, 738, 48
Bartelmann, M. & Schneider, P. 2001, Phys. Rep., 340, 291
Becker, M. R. & Kravtsov, A. V. 2011, ApJ, 740, 25
Bernstein, G. M., Armstrong, R., Krawiec, C., & March, M. C. 2016, MNRAS, 459, 4467
Bertin, E. 2006, in Astronomical Society of the Pacific Conference Series, Vol. 351, Astronomical Data Analysis Software and Systems XV, ed. C. Gabriel, C. Arviset, D. Ponz, & S. Enrique, 112
Bertin, E. 2011, in Astronomical Society of the Pacific Conference Series, Vol. 442, Astronomical Data Analysis Software and Systems XX, ed. I. N. Evans, A. Accomazzi, D. J. Mink, & A. H. Rots, 435
Bertin, E. & Arnouts, S. 1996, A&AS, 117, 393

Bertin, E., Mellier, Y., Radovich, M., et al. 2002, in Astronomical Society of the Pacific Conference Series, Vol. 281, Astronomical Data Analysis Software and Systems XI, ed. D. A. Bohlender, D. Durand, & T. H. Handley, 228
Bleem, L. E., Stalder, B., de Haan, T., et al. 2015, ApJS, 216, 27
Bradač, M., Ryan, R., Casertano, S., et al. 2014, ApJ, 785, 108
Broadhurst, T. J., Taylor, A. N., & Peacock, J. A. 1995, ApJ, 438, 49
Buddendiek, A., Schrabback, T., Greer, C. H., et al. 2015, MNRAS, 450, 4248
Daddi, E., Cimatti, A., Renzini, A., et al. 2004, ApJ, 617, 746
Diemer, B. & Kravtsov, A. V. 2015, ApJ, 799, 108
Dietrich, J. P., Böhnert, A., Lombardi, M., Hilbert, S., & Hartlap, J. 2012, MNRAS, 419, 3547
Erben, T., Schirmer, M., Dietrich, J. P., et al. 2005, Astronomische Nachrichten, 326, 432
Erben, T., Van Waerbeke, L., Bertin, E., Mellier, Y., & Schneider, P. 2001, A&A, 366, 717
Fenech Conti, I., Herbonnet, R., Hoekstra, H., et al. 2017, MNRAS, 467, 1627
Fort, B., Mellier, Y., & Dantel-Fort, M. 1997, A&A, 321, 353
Giallongo, E., Ragazzoni, R., Grazian, A., et al. 2008, A&A, 482, 349
Gilbank, D. G., Gladders, M. D., Yee, H. K. C., & Hsieh, B. C. 2011, AJ, 141, 94
Grogin, N. A., Kocevski, D. D., Faber, S. M., et al. 2011, ApJS, 197, 35
Hasselfield, M., Hilton, M., Marriage, T. A., et al. 2013, J. Cosmology Astropart. Phys., 7, 8
Heymans, C., Van Waerbeke, L., Bacon, D., et al. 2006, MNRAS, 368, 1323
Hinshaw, G., Larson, D., Komatsu, E., et al. 2013, ApJS, 208, 19
Hoag, A., Bradač, M., Huang, K. H., et al. 2015, ApJ, 813, 37
Hoekstra, H., Bartelmann, M., Dahle, H., et al. 2013, Space Sci. Rev., 177, 75
Hoekstra, H., Franx, M., & Kuijken, K. 2000, ApJ, 532, 88
Hoekstra, H., Franx, M., Kuijken, K., & Squires, G. 1998, ApJ, 504, 636
Hoekstra, H., Herbonnet, R., Muzzin, A., et al. 2015, MNRAS, 449, 685
Hoekstra, H., Viola, M., & Herbonnet, R. 2017, MNRAS, 468, 3295
Jarvis, M. & Jain, B. 2004, astro-ph/0412234 [astro-ph/0412234]
Jee, M. J., Dawson, K. S., Hoekstra, H., et al. 2011, ApJ, 737, 59
Jee, M. J., Hughes, J. P., Menanteau, F., et al. 2014, ApJ, 785, 20
Jee, M. J., Rosati, P., Ford, H. C., et al. 2009, ApJ, 704, 672
Kaiser, N. 2000, ApJ, 537, 555
Kaiser, N. & Squires, G. 1993, ApJ, 404, 441
Kaiser, N., Squires, G., & Broadhurst, T. 1995, ApJ, 449, 460
King, L. J., Clowe, D. I., Lidman, C., et al. 2002, A&A, 385, L5
Kissler-Patig, M., Pirard, J.-F., Casali, M., et al. 2008, A&A, 491, 941
Koekemoer, A. M., Fruchter, A. S., Hook, R. N., & Hack, W. 2003, in HST Calibration Workshop : Hubble after the Installation of the ACS and the NICMOS Cooling System, ed. S. Arribas, A. Koekemoer, & B. Whitmore, 337
Köhlinger, F., Hoekstra, H., & Eriksen, M. 2015, MNRAS, 453, 3107
Kuijken, K., Heymans, C., Hildebrandt, H., et al. 2015, MNRAS, 454, 3500
Le Fèvre, O., Tasca, L. A. M., Cassata, P., et al. 2015, A&A, 576, A79
Leauthaud, A., Massey, R., Kneib, J.-P., et al. 2007, ApJS, 172, 219
Leauthaud, A., Tinker, J., Bundy, K., et al. 2012, ApJ, 744, 159
LSST Dark Energy Science Collaboration. 2012, arXiv:1211.0310 [arXiv:1211.0310]
Luppino, G. A. & Kaiser, N. 1997, ApJ, 475, 20
Mandelbaum, R., Miyatake, H., Hamana, T., et al. 2017, PASJ subm. (also arXiv:1705.06745) [arXiv:1705.06745]
Martinez, P., Kolb, J., Tokovinin, A., & Sarazin, M. 2010, A&A, 516, A90
Massey, R., Hoekstra, H., Kitching, T., et al. 2013, MNRAS, 429, 661
Massey, R., Rhodes, J., Leauthaud, A., et al. 2007, ApJS, 172, 239
Massey, R., Schrabback, T., Cordes, O., et al. 2014, MNRAS, 439, 887
Masters, D. C., Stern, D. K., Cohen, J. G., et al. 2017, ApJ, 841, 111
Mayen, C. & Soucail, G. 2000, A&A, 361, 415
McCracken, H. J., Milvang-Jensen, B., Dunlop, J., et al. 2012, A&A, 544, A156
McInnes, R. N., Menanteau, F., Heavens, A. F., et al. 2009, MNRAS, 399, L84
Melchior, P., Viola, M., Schäfer, B. M., & Bartelmann, M. 2011, MNRAS, 412, 1552
Menanteau, F., Hughes, J. P., Sifón, C., et al. 2012, ApJ, 748, 7
Menanteau, F., Sifón, C., Barrientos, L. F., et al. 2013, ApJ, 765, 67
Meneghetti, M., Rasia, E., Vega, J., et al. 2014, ApJ, 797, 34
Merten, J., Meneghetti, M., Postman, M., et al. 2015, ApJ, 806, 4
Momcheva, I. G., Brammer, G. B., van Dokkum, P. G., et al. 2016, ApJS, 225, 27
Mroczkowski, T. 2011, ApJ, 728, L35
Muzzin, A., Marchesini, D., Stefanon, M., et al. 2013, ApJS, 206, 8
Navarro, J. F., Frenk, C. S., & White, S. D. M. 1997, ApJ, 490, 493
Neto, A. F., Gao, L., Bett, P., et al. 2007, MNRAS, 381, 1450
Planck Collaboration, Ade, P. A. R., Aghanim, N., et al. 2016, A&A, 594, A13
Postman, M., Coe, D., Benítez, N., et al. 2012, ApJS, 199, 25
Robitaille, T. & Bressert, E. 2012, APLpy: Astronomical Plotting Library in Python, Astrophysics Source Code Library
Rowe, B. T. P., Jarvis, M., Mandelbaum, R., et al. 2015, Astronomy and Computing, 10, 121
Schirmer, M. 2013, ApJS, 209, 21
Schneider, P. & Seitz, C. 1995, A&A, 294, 411
Schrabback, T., Applegate, D., Dietrich, J. P., et al. 2017, MNRAS accepted (https://doi.org/10.1093/mnras/stx2666) [arXiv:1611.03866]
Schrabback, T., Erben, T., Simon, P., et al. 2007, A&A, 468, 823
Schrabback, T., Hartlap, J., Joachimi, B., et al. 2010, A&A, 516, A63
Scoville, N., Aussel, H., Brusa, M., et al. 2007, ApJS, 172, 1
Seitz, C. & Schneider, P. 1997, A&A, 318, 687
Seitz, S. & Schneider, P. 1996, A&A, 305, 383
Sharon, K., Gladders, M. D., Marrone, D. P., et al. 2015, ApJ, 814, 21
Sifón, C., Menanteau, F., Hasselfield, M., et al. 2013, ApJ, 772, 25
Simon, P., Taylor, A. N., & Hartlap, J. 2009, MNRAS, 399, 48
Skelton, R. E., Whitaker, K. E., Momcheva, I. G., et al. 2014, ApJS, 214, 24
Skrutskie, M. F., Cutri, R. M., Stiening, R., et al. 2006, AJ, 131, 1163
Thölken, S., Schrabback, T., Reiprich, T. H., et al. 2017, A&A accepted (also arXiv:1708.07208) [arXiv:1708.07208]
Umetsu, K., Zitrin, A., Gruen, D., et al. 2016, ApJ, 821, 116
Viola, M., Kitching, T. D., & Joachimi, B. 2014, MNRAS, 439, 1909
von der Linden, A., Allen, M. T., Applegate, D. E., et al. 2014, MNRAS, 439, 2
Wright, C. O. & Brainerd, T. G. 2000, ApJ, 534, 34